The Meteoritical Society

Meteoritics & Planetary Science 55, Nr 9, 2044–2065 (2020)
doi: 10.1111/maps.13557

New constraints on the formation of lunar mafic impact melt breccias from S-Se-Te and highly siderophile elements

Philipp GLEIßNER* and Harry BECKER

Institut für Geologische Wissenschaften, Freie Universität Berlin, Malteserstr 74-100,12249Berlin, Germany
*Corresponding author. E-mail: gleissner@zedat.fu-berlin.de

(Received 05 December 2019; revision accepted 14 July 2020)

Abstract–Mass fractions of the siderophile volatile elements S, Se, and Te were determined together with highly siderophile elements (HSE) and osmium isotope ratios in multiple aliquots of five lunar mafic impact melt breccias. The impactites were sampled from presumably Imbrium-related ejecta deposits at the Apollo 14, 15, and 16 landing sites. As in many mafic impact melt breccias, all studied impactites display fractionated siderophile element patterns characteristic of differentiated metal, interpreted to reflect metal-rich impactor material from the core of a differentiated planetesimal. The compositional record of Fra Mauro crystalline matrix breccias and recent constraints on the time of their formation suggest that the admixture of this differentiated metal component to the Procellarum KREEP Terrane occurred before the Imbrium basin was formed. The impact melt rock portion of dimict breccia 61015 displays fractionations of HSE like other mafic impact melt breccias, but CI chondrite-like ratios of S, Se, Te, and Ir. Preservation of these contrasting impactor signatures in a single impactite sample demonstrates mixing of differentiated metal and CI chondrite-like impactor material and their homogenization in an impact melt sheet. Correlations of highly siderophile element ratios between impactites from different Apollo landing sites suggest that siderophile element inventories of many lunar impactites were affected by similar mixing processes. Mass fractions and ratios of S, Se, and Te in other mafic impact melt breccias closely resemble those of pristine mafic target rocks.

INTRODUCTION

Analyses of lunar impactites provide insights into the compositional spectrum of impactor materials and the time of their accretion. For the time before ~3.8 Ga, no similar record is available from any other solar system object. This is mainly due to the incomplete sampling of asteroids by meteorites and the destructive power of surface processes on terrestrial planets. On Earth, most of the material that accreted after its core was fully formed (late accreted material) was recycled into the mantle. In order to constrain compositional aspects of late accreting material from the time-integrated record of the present-day terrestrial mantle, many processes must be deciphered. Therefore, the lunar record of late accretion is an important constraint for our understanding of the last stage of planetary accretion in the inner solar system. Important compositional parameters for the evolution of terrestrial planets and minor bodies may have been set during this stage (e.g., oxygen fugacity and availability of volatiles like H_2O, C, S).

Constraints on the nature of late accreted matter come mainly from siderophile elements. Because of their strong solubility preference for iron metal, core formation strongly depleted the silicate portion of differentiated bodies in highly siderophile elements (HSE). Therefore, significant later addition of HSE-rich material (e.g., chondritic meteorites) leaves a chemical trace in the composition of planetary silicate reservoirs (e.g., Walker et al. 2015). In contrast to HSE, the inventory of less siderophile and more volatile elements (SVE) is controlled by a more complex interplay between core formation, late accretion, and volatilization (e.g., Righter et al. 2018). However, if the latter processes can be deciphered, SVE can provide a

© 2020 The Authors. Meteoritics & Planetary Science published by Wiley Periodicals LLC on behalf of The Meteoritical Society (MET)
This is an open access article under the terms of the Creative Commons Attribution License, which permits use, distribution and reproduction in any medium, provided the original work is properly cited.

record of the volatile content of late accreted matter, information which is not easily retrieved from the composition of HSE alone. For example, studies of SVE like S, Se, and Te in terrestrial mantle rocks reveal similarities in element and isotopic ratios to carbonaceous chondrites and suggest that carbonaceous chondrite-like material (i.e., volatile-rich primitive material) was accreted to Earth at various stages (e.g., Wang and Becker 2013; Braukmüller et al. 2019; Varas-Reus et al. 2019).

Recent determinations of highly and moderately volatile element mass fractions in different lunar lithologies reveal that the Moon may not be as much depleted in volatiles as previously thought and significant amounts of volatiles may have been accreted late (e.g., Hauri et al. 2015). The siderophile element inventory of lunar samples was studied since the first Apollo mission samples became available, mainly by radiochemical neutron activation analysis (RNAA). However, only a few HSE could be analyzed and some key elements like sulfur were often not included at that time (e.g., Keays et al. 1974). More recently, isotope dilution in combination with inductively coupled plasma mass spectrometry (ICP-MS) has been applied to study HSE in lunar lithologies (e.g., Norman et al. 2002; Puchtel et al. 2008; Day et al. 2010). Lunar mare basalts are generally low in HSE, but display approximately chondritic element ratios, interpreted as indicative of a small fraction of a chondritic component in the lunar mantle, which may have accreted during the magma ocean stage (Day and Walker 2015). Crustal impactites, which subsequently formed during bombardment of the lunar highlands, display chondritic to variably fractionated HSE patterns (Norman et al. 2002; Puchtel et al. 2008; Fischer-Gödde and Becker 2012; Sharp et al. 2014; Liu et al. 2015; Gleißner and Becker 2017, 2019). The latter are mainly observed in mafic impact melt breccias and were attributed to accretion of chemically fractionated planetesimal or embryo core material (Fischer-Gödde and Becker 2012; Gleißner and Becker 2017). Because the HSE fractionation among bulk chondrites is small (e.g., Horan et al. 2003; Fischer-Gödde et al. 2010) and patterns and abundances of HSE in mafic impact melt breccias are biased by the differentiated metal component, there are limits to the discrimination of small mass fractions of distinct primitive material in polymict impactites. In contrast, fractionations among the chalcogens S, Se, and Te in carbonaceous versus noncarbonaceous chondrites are larger and in principle offer more promise for the identification of impactor types.

Here, we present the first combined data set for HSE and moderately siderophile and volatile S, Se, and Te in lunar impactites, determined with isotope dilution mass spectrometry methods. In order to unravel the siderophile element distribution in individual impactites, we determined HSE, S, Se, and Te abundances and $^{187}Os/^{188}Os$ ratios from the same aliquot of multiple subsamples of five impactites. The combined data set sheds new light on the inventory and behavior of siderophile elements of different volatility in lunar impactites. Furthermore, it places new constraints on the composition and volatile content of impactor materials, their time of accretion to the lunar surface, and mixing of these materials at various scales.

LUNAR IMPACTITE SAMPLES OF THIS STUDY

Samples of this study are ancient mafic impact melt breccias, sampled from the Fra Mauro Formation of the Apollo 14 (14305), the Apennine Front of the Apollo 15 (15405, 15445), and the Cayley Formation of the Apollo 16 (61015, 62235) landing sites. All three geologic units are ejecta deposits that were interpreted to be the result of the impact event that formed the Imbrium basin (e.g., Ryder and Bower 1977; Norman et al. 2010; Snape et al. 2016). Mafic impact melt breccias differ from the composition of the feldspathic upper crust of the Moon in their Mg- and Fe-rich major element composition and decidedly in their KREEP-rich composition (KREEP = rich in lithophile incompatible trace elements like potassium, rare earth elements, and phosphorus). Therefore, it appears very likely that all of them were formed within the Procellarum KREEP Terrane, a unique geochemical province on the lunar near side (Haskin et al. 1998; Korotev 2000). Based on abundant Ar-Ar ages around ~3.9 Ga and the common occurrence of Fe-Ni metal with suprachondritic Au/Ir ratios, it was suggested that most of these breccias were formed by impact of a single iron meteorite, which is believed to represent the composition of the Imbrium impactor (Haskin et al. 1998; Korotev 2000).

Sample 14305 is a crystalline matrix breccia, comprising roughly 30 vol% lithic clasts, ranging from 10 cm down to the grain size of the fine-grained matrix. The dominant clast lithology is a dark gray aphanitic microbreccia, but a number of different basaltic and feldspathic highland clasts also occur (Carlson and Walton 1978; Shervais et al. 1983). The bulk breccia is enriched in lithophile trace elements and displays a typical KREEP pattern (Fig. S1 in supporting information). According to RNAA data, the microbreccia lithology is KREEP-rich and characterized by high and fractionated HSE abundances and a slight depletion of Se when compared to the HSE (Fig. S2a in supporting information). We analyzed a subsample of

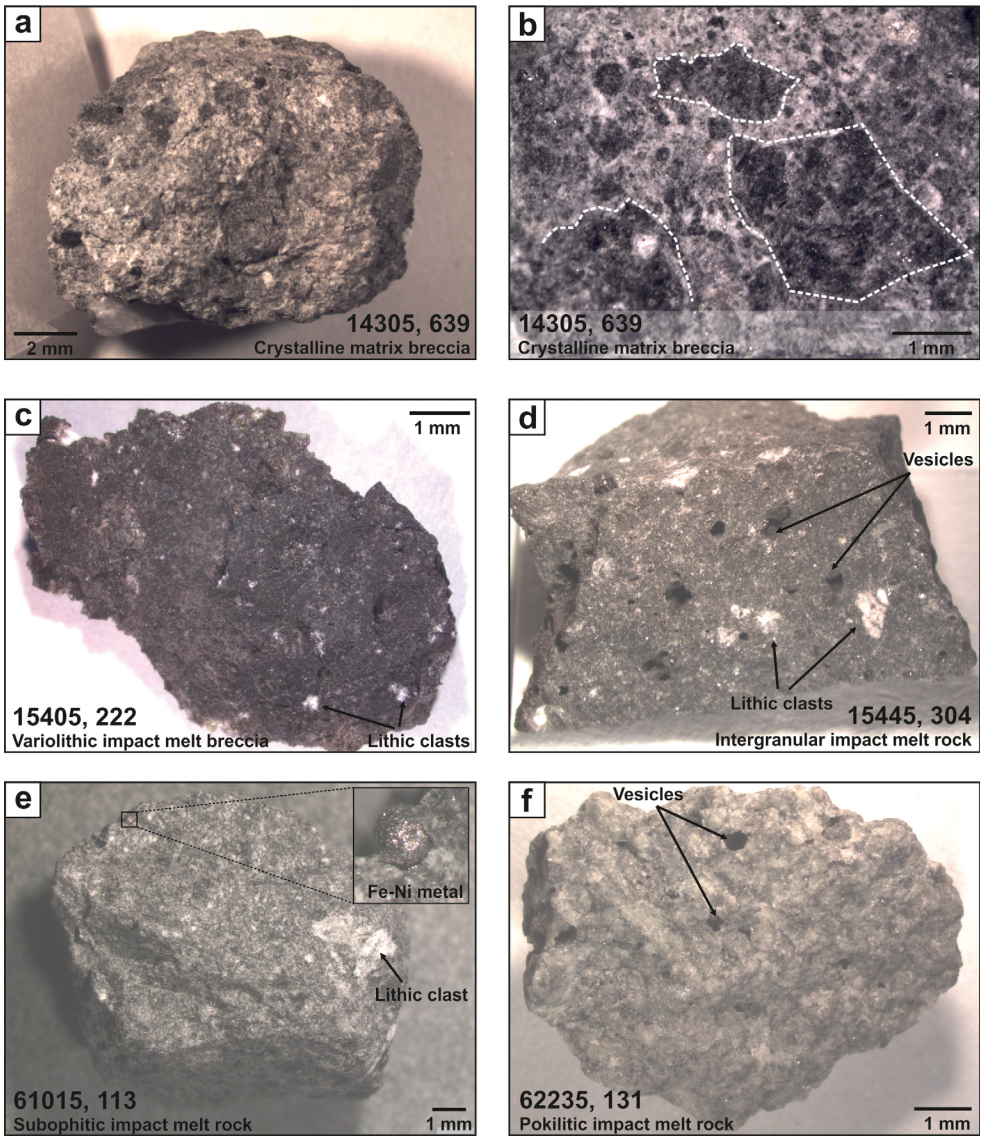

Fig. 1. Mafic impact melt breccias examined in this study. a) Crystalline matrix breccia 14305. b) Angular dark gray microbreccia clasts in light gray matrix of 14305. c) Impact melt breccia 15405, displaying bright lithic clasts. d) Impact melt rock portion of "black and white rock" 15445. e) Very high alumina impact melt rock portion of dimict breccia 61015. f) Mafic poikilitic impact melt rock 62235. (Color figure can be viewed at wileyonlinelibrary.com.)

14305, 611 (0.914 g). The sample is composed of angular fragments of the dark microbreccia lithology ranging from mm- to μm-size (Fig. 1a), in a brecciated matrix (Fig. 1b). The well-studied crystalline matrix breccia 14321, very similar to 14305 in texture (Carlson and Walton 1978), clast population (Shervais et al. 1983), and trace element composition (Fig. S2b) have been analyzed for HSE with isotope dilution mass spectrometry methods by Puchtel et al. (2008). Snape et al. (2016) determined ^{207}Pb-^{206}Pb ages of 3.926–3.944 Ga in phosphates from 14305, 14321, and similar breccias of the Fra Mauro Formation. These dates were interpreted as complete or partial resetting of the U-Pb system in phosphates due to heating related to the Imbrium event.

Sample 15405 is a fine-grained, very KREEP-rich impact melt breccia, which contains a clast population of KREEP basalts, quartz monzodiorites, and alkali suite rocks welded together in a variolithic and flow banded matrix (e.g., Lindstrom et al. 1988; Grange et al. 2013). Its bulk composition is found to be similar to that of Apollo 15 KREEP basalts (Lindstrom et al. 1988), but contains higher amounts of meteoritic siderophiles (Fig. S2c). U-Pb dating of zircons and phosphates reveal a complex crystallization and resetting history with the last thermal events interpreted

as impact-induced mineral-melt reactions at 1.94 ± 0.01 Ga and subsequent partial Pb-loss at the time of a second impact at 1.407 ± 0.057 Ga (Grange et al. 2013). We analyzed a subsample of 15405, 6 (0.984 g). The black-gray breccia is fine-grained with some vesicles and comprises mm-sized bright lithic clasts with frayed outlines (Fig. 1c).

Sample 15445 is one of two prominent Apollo 15 breccias with abundant white lithic clasts in a dark and fine-grained impact melt rock matrix ("black and white rocks"). The impact melt rock portion of both, 15445 and 15455, is basaltic in composition with intermediate enrichment of lithophile trace elements (Fig. S1), previously termed as low-K Fra Mauro basalt composition and regarded as the most likely candidate for Imbrium basin impact melt (e.g., Ryder and Bower 1977; Lindstrom et al. 1988). However, Ar-Ar data from different splits of both "black and white rocks" consistently show disturbed release patterns exhibiting no real plateau (Seifert et al. [2017] and references therein). The impact melt rock matrix is an aggregate of silicates in intergranular texture with accessory troilite, which forms blebs around metal grains or occurs as tiny discrete particles in the matrix or associated with vesicles (Ryder and Bower 1977). Large, cm-size lithic clasts and abundant mineral clasts are derived from norites and troctolites of the Mg-suite (Ryder and Bower 1977; Spudis et al. 1991). RNAA data (Fig. S2d) and more recent isotope dilution mass spectrometry data (Liu et al. 2015) reveal very similar concentrations of siderophile elements in impact melt rock portions of both samples. In the present work, a piece of subsample 15445,0 (0.888 g) was studied. The impact melt rock displays a fine- to medium-grained interlocked texture with angular lithic clasts and irregular vesicles (Fig. 1d).

Sample 61015 is a dimict breccia which consists of shocked ferroan anorthosite intruded by very high alumina basaltic impact melt (group 2DB of Korotev 1994). The impact melt rock portion displays mainly recrystallized fine-grained intersertal to subophitic texture with some mesostasis, but sometimes also glassy parts. No compositional differences were observed between the textural variants of the melt rock except those produced by heterogeneous distribution of metal particles or plagioclase microphenocrysts (James et al. 1984). Lithophile incompatible trace elements are moderately enriched and show a typical KREEP-like pattern (Fig. S1). Earlier RNAA data of the impact melt portion yield one to two orders of magnitude higher Se, Te, and HSE contents when compared to the anorthositic portion (Fig. S2e). The clast population of the impact melt portion is mainly derived from the anorthosite portion of the sample. Therefore, its formation is interpreted in the context of melt injection into the floor of a larger crater (James et al. 1984). Norman et al. (2006) reported an Ar-Ar age of 3.899 ± 0.036 Ga (corrected to 3.932 ± 0.036 Ga according to the new fluence monitor calibration of Renne et al. 1998) for the impact melt rock portion and tentatively proposed that dimict breccias represent the oldest breccia group sampled at the Apollo 16 site. We analyzed a subsample of 61015, 82 (0.787 g) from the impact melt rock portion. The fine-grained subophitic rock contains sparse mm-sized white clasts and metal globules up to 250 μm in diameter (Fig. 1e).

Sample 62235 is a homogeneous mafic pokilitic impact melt rock (group 1F of Korotev 1994) with a high KREEP fraction (Fig. S1). Medium-grained orthopyroxene oikocrysts enclose plagioclase laths whereas accessory phases like ilmenite, troilite, and Fe-Ni metal occur between the oikocrysts (McGee et al. 1979). The clast population is dominated by shocked and partially annealed plagioclase whereas minor subophitic textured areas are interpreted as lithic clasts of either basaltic (McGee et al. 1979) or impact melt rock origin (Reimold and Borchardt 1984). Norman et al. (2006) determined an Ar-Ar age of 3.876 ± 0.032 Ga (corrected to 3.909 ± 0.032 Ga according to the new fluence monitor calibration of Renne et al. 1998) and proposed that seven mafic pokilitic melt breccias with similar ages formed in the same impact event. Available RNAA data for mafic poikilitic melt breccias display very similar absolute and relative abundances of siderophile and lithophile trace elements (Fig. S2f). We studied two pieces of subsample 62235, 61 (0.854 g in total). Both splits display medium-grained poikilitic texture with visible pyroxene, plagioclase, and ilmenite crystals, and irregular vesicles (Fig. 1f).

ANALYTICAL METHODS

Sample preparation, digestion, chemical separation, and analyses were conducted in the geochemistry laboratories at Freie Universität Berlin, Germany, following procedures for HSE and chalcogens established previously for terrestrial rocks, lunar samples, and chondrites (Fischer-Gödde et al. 2010; Fischer-Gödde and Becker 2012; Wang and Becker 2013, 2014; Gleißner and Becker 2017, 2019). The procedure will be outlined briefly. For a more detailed description, the reader is referred to the aforementioned publications.

Samples were broken into small chips in a laminar flow hood, using an alumina ceramic mortar and pestle. For each sample, 10 aliquots of 55–120 mg were weighed into quartz glass digestion vessels and appropriate amounts of mixed ^{185}Re-^{190}Os, ^{99}Ru-^{105}Pd-^{191}Ir-^{194}Pt, ^{77}Se-^{125}Te, and individual ^{34}S

spike solution were added. Sample digestion was carried out in a high-pressure asher (Anton Paar) using 3 mL reverse *aqua regia* at 10 MPa and 320 °C for 16 h. All devices like mortars, high pressure asher vessels, columns, and beakers were used for lunar samples only.

After digestion, Os was immediately extracted from the digestion solution into chloroform and further purified by microdistillation. For five aliquots of each sample, the digestion solution was split into 70% for HSE and 30% for the chalcogens. The HSE fraction was converted to chloride form and then dissolved in 0.5 M HCl-60% acetone. Rhenium, Ir, Ru, Pt, Rh, and Au were separated from the matrix by cation exchange chromatography using 10 mL pre-cleaned Eichrom 50W-X8 resin (100–200 mesh; Fischer-Gödde and Becker 2012; Gleißner and Becker 2017, 2019). Cadmium, which interferes on some Pd masses, was removed by cation exchange chromatography in 0.2 M HCl using 1.7 mL Eichrom 50W-X8 resin (100–200 mesh) from all aliquots of samples 14305 and 15405 (Fischer-Gödde et al. 2010). In contrast to previous studies, samples 14305, 15405, 15445, and 62235 are very KREEP-rich, which required the following additional separation steps. In order to prevent possible interferences from TmO and YbO on Re masses, we conducted an Re cleanup in 0.8 M HNO_3 using 0.25 mL Eichrom 1-X8 anion resin (100–200 mesh; Becker et al. 2001). Zirconium, which forms oxides that interfere on even Pd masses, was removed in 1 M HCl on 2 mL Eichrom LN Spec resin (100–150 μm; Chu et al. 2015). The S-Se-Te fraction was treated with concentrated HCl to reduce Se and Te to their tetravalent state and a two-step ion exchange chromatographic procedure was applied (Wang and Becker 2013, 2014). In the first step, S, Se, and Te were separated from iron and other matrix elements on 2 mL Eichrom 1-X8 anion resin (100–200 mesh). The collected Te fraction was ready for mass spectrometric measurement whereas a second cleanup step on 1 mL Eichrom 50W-X8 cation resin (100–200 mesh) was necessary for the S-Se fraction.

Osmium isotopic ratios were determined as OsO_3^- by negative thermal ionization mass spectrometry using a Thermo-Finnigan Triton instrument. Signals were detected using an electron multiplier (SEM) in pulse counting mode or on Faraday cups in static mode. Measured isotope ratios were corrected for interferences from isobaric OsO_3^- molecules and instrumental mass fractionation using a linear fractionation law and an $^{192}Os/^{188}Os$ ratio of 3.08271 (Luck and Allègre 1983). Repeated measurements of the University of Maryland Os standard solution yielded $^{187}Os/^{188}Os$ of 0.11403 ± 0.00012 (2 SD, $n = 15$) on SEM and 0.11380 ± 0.00007 (2 SD, $n = 10$) using Faraday cups. For improved precision of $^{187}Os/^{188}Os$ ratios, we analyzed each sample aliquot twice on separate filaments and we report mean values and mean/$\sqrt{2}$ uncertainties (except for 15405 where low Os concentrations allowed only one analysis per aliquot).

All other elements were analyzed by sector-field ICP-MS using a Thermo-Electron Element-XR instrument. HSE sample solutions were introduced using a Scott-type spray chamber for Re, Ir, Pt, Au, or an Aridus I desolvation system for Ir, Ru, Pt, Rh, Pd and signals were detected in low resolution mode with an SEM. Oxide formation fractions (CeO/Ce) were 5–10% for measurements using a Scott-type spray chamber and 0.25–0.5% using the Aridus I desolvator. Cadmium, Hg, and Os isotopes were analyzed to monitor isobaric interferences and such interferences were corrected when necessary. Zirconium, Hf, Tm, Yb, Lu, Ta, Y, Rb, and Sr were monitored for evaluation of potentially interfering oxide species. Because the above-described element separation protocols were used, isobaric interferences were mostly negligible (exceptions are noted in Table 1). According to previous estimates of element concentrations in KREEP (Warren 1989), very KREEP-rich impactites may be slightly enriched in Cu and Zn when compared to average lunar impactites and lunar crust (Haskin and Warren 1991). In order to evaluate the interference potential of CuAr (on Rh and Pd) and ZnAr (on Pd), we monitored Cu and Zn in the Pd cut after cation exchange chemistry, but found negligible mass fractions. The sulfur sample solution was introduced using a conventional Scott-type spray chamber and detected in medium resolution in order to avoid inferences from O_2^+ and HS^+. Nickel and Zn were monitored, but interferences from double charged ions were insignificant. Selenium and Te solutions were introduced via hydride generation using a double pass Scott-type spray chamber and detected in low resolution mode (Wang and Becker 2013, 2014). During hydride generation measurements, the background was found to be very stable and signal/background ratios for unspiked isotopes range between 4 and 90.

The internal precision of measured isotope ratios ranges from 0.1% to 1% ($2\sigma_m$). Instrumental mass discrimination was determined and corrected by comparison of isotope ratios with standard solutions measured in the same sequence. Isotopic ratios of $^{32}S/^{34}S$, $^{77}Se/^{82}Se$, $^{99}Ru/^{101}Ru$, $^{105}Pd/^{108}Pd$, $^{125}Te/^{126}Te$, $^{185}Re/^{187}Re$, $^{191}Ir/^{193}Ir$, and $^{194}Pt/^{195}Pt$ were used for isotope dilution calculations. The isotope ratios $^{32}S/^{33}S$, $^{77}Se/^{78}Se$, $^{105}Pd/^{106}Pd$, and $^{194}Pt/^{196}Pt$ were determined for control of consistency and possible interferences. Concentrations of monoisotopic Rh and Au were determined via a combined internal/external standardization technique for the $^{197}Au/^{193}Ir$ and

Table 1. Highly siderophile and chalcogen element concentrations and osmium isotope ratios of mafic impact melt breccias.

	Weight (g)	Re (ng g^{-1})	Re* (ng g^{-1})	Os (ng g^{-1})	Ir (ng g^{-1})	Ru (ng g^{-1})	Pt (ng g^{-1})	Rh (ng g^{-1})	Pd (ng g^{-1})	Au (ng g^{-1})	Te (ng g^{-1})	Se (ng g^{-1})	S (μg g^{-1})	$^{187}Os/^{188}Os$	$^{187}Re/^{188}Os$
Crystalline matrix breccia 14305, 639															
14305#1	0.07908	0.498 (38)	0.508	4.92 (1)	4.99 (3)	10.1 (1)	12.8 (3)	2.41	11.1 (5)	4.21	n.a.	n.a.	n.a.	0.1346 (6)	0.488 (37)
14305#2	0.07923	0.428 (38)	0.421	4.14 (1)	4.36 (3)	8.63 (4)	11.0 (3)	1.94	9.32 (46)	3.55	n.a.	n.a.	n.a.	0.1340 (7)	0.499 (44)
14305#3	0.07988	0.484 (37)	0.482	4.70 (1)	4.36 (3)	8.74 (3)	11.0 (3)	2.10	9.20 (45)	3.45	n.a.	n.a.	n.a.	0.1343 (6)	0.497 (38)
14305#4	0.08585	0.582 (35)	0.487	4.69 (1)	4.82 (4)	9.95 (5)	12.7 (3)	2.62	11.1 (4)	4.70	n.a.	n.a.	n.a.	0.1348 (6)	0.599 (36)
14305#5	0.08541	0.390 (35)	0.364	3.48 (1)	3.59 (3)	7.42 (5)	9.51 (3)	1.84	9.26 (42)	3.34	n.a.	n.a.	n.a.	0.1351 (8)	0.540 (49)
14305#6	0.10206	0.610 (29)	0.471	4.56 (1)	4.68 (4)	9.48 (6)	12.3 (3)	2.16	10.1 (4)	3.76	9.6 (2.7)	159 (41)	920 (125)	0.1346 (5)	0.645 (31)
14305#7[a]	0.10137	0.454 (29)		n.a.	4.48 (5)	9.06 (6)	11.4 (3)	1.79	9.08 (36)	3.68	n.a.	n.a.	n.a.	n.a.	
14305#8	0.08836	0.517 (34)	0.515	4.90 (1)	4.87 (6)	9.90 (11)	13.0 (3)	2.54	10.6 (4)	3.76	4.30 (95)	124 (30)	875 (134)	0.1353 (6)	0.509 (33)
14305#9	0.10629	0.563 (28)	0.481	4.73 (1)	4.77 (7)	9.55 (9)	12.6 (3)	2.25	10.2 (3)	3.19	3.27 (78)	114 (23)	812 (113)	0.1340 (5)	0.574 (29)
14305#10	0.10658	0.586 (28)	0.583	5.56 (1)	5.72 (8)	10.9 (1)	14.4 (3)	2.67	11.0 (3)	5.06	3.63 (87)	101 (18)	782 (112)	0.1352 (4)	0.508 (24)
Av. #1-#10		0.516 (34)	0.482	4.66 (1)	4.69 (5)	9.42 (7)	12.1 (3)	2.24	10.1 (4)	3.88				0.1347 (3)	0.543 (36)
Av. #6-#10[a]		0.571 (30)	0.513	4.94 (1)	5.02 (6)	9.97 (9)	13.1 (3)	2.40	10.5 (4)	3.95	5.18 (95)	124 (27)	845 (120)	0.1348 (6)	0.560 (65)
Variolithic impact melt breccia 15405, 222															
15405#1	0.07342	b.d.l.	0.044	0.501 (11)	0.614 (20)	1.14 (3)	1.23 (33)	0.456	n.d.	0.420	n.a.	n.a.	n.a.	0.1290 (87)	
15405#2	0.08795	0.078 (34)	0.035	0.415 (9)	0.481 (16)	0.845 (23)	0.98 (27)	0.261	n.d.	0.300	n.a.	n.a.	n.a.	0.1276 (87)	0.90 (40)
15405#3	0.09319	0.093 (32)	0.062	0.715 (9)	0.835 (16)	1.44 (2)	1.68 (26)	0.333	n.d.	0.466	n.a.	n.a.	n.a.	0.1280 (48)	0.63 (22)
15405#4	0.08624	b.d.l.	0.045	0.514 (9)	0.580 (17)	0.951 (24)	0.96 (28)	0.150	0.95 (42)	0.425	n.a.	n.a.	n.a.	0.1285 (72)	
15405#5	0.08096	b.d.l.	0.033	0.385 (10)	0.640 (18)	0.900 (25)	0.93 (30)	0.163	n.d.	0.295	n.a.	n.a.	n.a.	0.128 (10)	
15405#6	0.08466	b.d.l.	0.043	0.500 (8)	0.568 (15)	0.992 (21)	1.12 (24)	0.252	1.18 (36)	0.502	7.5 (2.2)	163 (119)	731 (104)	0.1280 (64)	
15405#7	0.10654	b.d.l.	0.042	0.489 (8)	0.589 (14)	1.04 (2)	1.23 (23)	0.240	n.d.	0.417	2.92 (92)	{81 (43)}	587 (98)	0.1279 (62)	
15405#8	0.08931	0.058 (31)	0.043	0.503 (8)	0.582 (15)	1.04 (2)	1.21 (25)	0.375	n.d.	0.333	5.9 (1.7)	{86 (55)}	779 (109)	0.1280 (66)	0.56 (30)
15405#9	0.08731	0.031 (26)	0.036	0.418 (7)	0.507 (13)	0.924 (19)	1.06 (21)	0.195	0.99 (31)	0.313	b.d.l.	{83 (38)}	559 (91)	0.1281 (66)	0.36 (30)
15405#10[b]	0.10396	b.d.l.	0.034	0.382 (11)	0.461 (19)	0.795 (28)	2.11 (32)	0.335	2.38 (48)	0.485	5.2 (1.6)	{99 (55)}	726 (139)	0.129 (11)	
Av. #1-#10		0.065 (35)	0.042	0.482 (9)	0.584 (17)	1.01 (2)	1.16 (27)	0.275	1.04 (37)	0.398				0.1282 (3)	0.61 (22)
Av. #6-#10		0.045 (31)	0.040	0.457 (9)	0.541 (15)	0.956 (23)	1.16 (23)	0.280	1.08 (34)	0.412	5.2 (1.6)	101 (58)	675 (110)	0.1282 (3)	0.46 (19)
Intergranular impact melt rock 15445, 304															
15445#1	0.07071	0.452 (17)	0.433	4.04 (1)	4.05 (3)	8.97 (5)	10.3 (3)	1.84	10.4 (5)	4.76	n.a.	n.a.	n.a.	0.1362 (4)	0.540 (21)
15445#2	0.09029	0.535 (14)	0.442	4.09 (1)	4.01 (3)	8.88 (6)	10.7 (3)	2.46	11.2 (4)	4.89	n.a.	n.a.	n.a.	0.1365 (3)	0.632 (16)
15445#3	0.08555	0.632 (14)	0.603	5.63 (1)	5.58 (4)	12.1 (1)	14.5 (3)	2.36	n.d.	6.43	n.a.	n.a.	n.a.	0.1361 (3)	0.541 (12)
15445#4	0.07395	0.608 (16)	0.587	5.48 (1)	5.38 (3)	12.2 (1)	14.4 (3)	2.53	14.0 (5)	6.36	n.a.	n.a.	n.a.	0.1361 (3)	0.535 (15)
15445#5	0.09592	0.662 (13)	0.639	5.98 (1)	5.83 (3)	12.6 (1)	15.0 (3)	2.55	13.8 (4)	6.25	n.a.	n.a.	n.a.	0.1359 (3)	0.533 (10)
15445#6[c]	0.08466		0.427	3.95 (1)	3.89 (3)	8.86 (4)	10.5 (3)	1.91	10.2 (4)	3.66	{1.56 (83)}	{112 (41)}	586 (123)	0.1364 (4)	
15445#7	0.10654	0.340 (11)	0.319	3.18 (1)	3.05 (3)	6.52 (3)	7.77 (23)	1.41	8.15 (34)	2.85	{1.19 (68)}	{106 (33)}	544 (97)	0.1336 (4)	0.516 (17)
15445#8	0.08931	0.529 (14)	0.482	4.51 (1)	4.40 (3)	9.61 (5)	13.3 (3)	2.21	11.4 (4)	4.37	{1.07 (78)}	{122 (38)}	634 (116)	0.1359 (3)	0.566 (15)
15445#9	0.08731	0.637 (14)	0.610	5.71 (1)	5.41 (3)	12.2 (1)	14.6 (3)	2.39	13.3 (4)	5.07	{1.53 (86)}	{108 (34)}	654 (119)	0.1359 (3)	0.538 (12)
15445#10	0.10396	0.697 (12)	0.661	6.13 (1)	5.99 (3)	13.2 (1)	15.6 (2)	2.38	14.1 (4)	6.03	{3.8 (1.6)}	128 (42)	609 (100)	0.1364 (2)	0.548 (9)
Av. #1-#10		0.565 (14)	0.520	4.87 (1)	4.76 (3)	10.5 (1)	12.7 (3)	2.20	11.8 (4)	5.03				0.1359 (5)	0.550 (22)
Av. #6-#10		0.546 (13)	0.499	4.69 (1)	4.54 (3)	10.0 (1)	12.3 (3)	2.05	11.4 (4)	4.40	1.9 (1.0)	115 (37)	603 (110)	0.1358 (11)	0.541 (21)
Subophitic impact melt rock 61015, 113															
61015#1	0.06265	1.54 (2)	1.56	13.5 (1)	14.6 (1)	31.3 (1)	39.8 (4)	6.84	33.8 (6)	12.0	55.3 (2.3)	371 (57)	961 (132)	0.1392 (2)	0.549 (7)
61015#2	0.06234	0.464 (20)	0.442	3.50 (1)	4.01 (1)	11.7 (1)	13.7 (4)	3.06	15.8 (6)	7.39	40.3 (2.1)	382 (61)	1030 (135)	0.1435 (6)	0.641 (27)
61015#3	0.06752	1.02 (2)	1.01	8.64 (1)	9.57 (1)	22.0 (1)	28.0 (4)	4.93	24.9 (5)	13.4	54.0 (3.9)	372 (63)	914 (123)	0.1399 (3)	0.573 (10)
61015#4	0.07420	0.572 (16)	0.565	4.84 (1)	5.34 (1)	12.3 (1)	15.2 (3)	2.72	14.0 (5)	6.84	25.8 (1.7)	324 (53)	789 (117)	0.1398 (4)	0.571 (16)
61015#5	0.07690	0.463 (16)	0.455	4.00 (1)	4.32 (1)	9.73 (1)	12.1 (3)	2.43	11.6 (5)	5.48	42.9 (5)	301 (47)	743 (109)	0.1386 (4)	0.558 (19)
61015#6[c]	0.07080		2.72	25.1 (1)	26.3 (1)	46.5 (1)	62.3 (4)	9.41	41.6 (6)	15.5	n.a.	n.a.	n.a.	0.1365 (1)	
61015#7[c]	0.10746		0.260	2.23 (1)	2.46 (1)	5.96 (1)	7.31 (2)	1.45	6.99 (34)	2.80	n.a.	n.a.	n.a.	0.1398 (5)	
61015#8[c]	0.09878		0.854	7.22 (1)	7.95 (1)	19.2 (1)	23.7 (2)	4.38	22.6 (4)	9.48	n.a.	n.a.	n.a.	0.1404 (2)	
61015#9[c]	0.09422		5.04	45.9 (1)	47.5 (2)	92.2 (2)	121 (4)	20.0	90.9 (1.0)	34.2	n.a.	n.a.	n.a.	0.1371 (1)	
61015#10[c]	0.07241		3.17	28.2 (1)	29.7 (1)	61.0 (1)	79.0 (4)	13.6	62.3 (7)	25.7	n.a.	n.a.	n.a.	0.1382 (1)	

Table 1. *Continued*. Highly siderophile and chalcogen element concentrations and osmium isotope ratios of mafic impact melt breccias.

	Weight (g)	Re (ng g^{-1})	Re* (ng g^{-1})	Os (ng g^{-1})	Ir (ng g^{-1})	Ru (ng g^{-1})	Pt (ng g^{-1})	Rh (ng g^{-1})	Pd (ng g^{-1})	Au (ng g^{-1})	Te (ng g^{-1})	Se (ng g^{-1})	S (μg g^{-1})	$^{187}Os/^{188}Os$	$^{187}Re/^{188}Os$
Av. #1-#10			1.63	14.5 (1)	15.3 (1)	31.5 (1)	40.5 (6)	6.95	32.7 (8)	13.3				0.1380 (12)	
Av. #1-#5		0.793 (22)	0.787	6.74 (1)	7.38 (1)	17.0 (1)	21.2 (4)	3.90	19.6 (6)	8.86	43.2 (3.1)	347 (56)	878 (123)	0.1398 (17)	0.577 (32)
Pokilitic impact melt rock 62235, 131															
62235#1	0.07561	1.40 (2)	1.36	12.4 (1)	13.5 (1)	29.9 (1)	37.3 (3)	6.41	34.7 (5)	16.9	n.a.	n.a.	n.a.	0.1370 (2)	0.545 (6)
62235#2	0.06367	1.40 (2)	1.25	11.5 (1)	12.4 (1)	27.0 (1)	33.7 (4)	5.75	32.1 (6)	12.0	n.a.	n.a.	n.a.	0.1367 (2)	0.590 (8)
62235#3	0.07751	1.70 (2)	1.33	12.3 (1)	13.3 (1)	28.1 (1)	35.4 (3)	5.95	31.5 (5)	12.4	n.a.	n.a.	n.a.	0.1366 (2)	0.666 (6)
62235#4	0.06477	1.53 (2)	1.46	13.3 (1)	14.6 (1)	31.5 (1)	39.4 (4)	7.28	36.0 (6)	16.6	n.a.	n.a.	n.a.	0.1370 (2)	0.553 (7)
62235#5	0.05474	1.64 (2)	1.45	13.1 (1)	14.4 (1)	30.5 (1)	42.7 (4)	6.24	34.6 (7)	14.7	n.a.	n.a.	n.a.	0.1373 (2)	0.601 (8)
62235#6	0.09311	1.42 (1)	1.36	12.6 (1)	14.3 (1)	30.0 (1)	37.9 (3)	6.27	33.0 (5)	12.3	3.57 (89)	260 (33)	855 (113)	0.1366 (2)	0.544 (5)
62235#7	0.08832	1.48 (1)	1.19	10.9 (1)	12.4 (1)	26.7 (1)	33.8 (3)	5.80	31.3 (5)	14.0	2.84 (79)	251 (43)	898 (120)	0.1370 (2)	0.657 (6)
62235#8	0.11080	1.86 (1)	1.57	14.3 (1)	16.2 (1)	34.4 (1)	43.5 (2)	7.27	37.8 (5)	15.6	3.68 (70)	290 (37)	1222 (102)	0.1370 (2)	0.625 (4)
62235#9	0.10200	1.45 (1)	1.34	12.3 (1)	14.1 (1)	30.3 (1)	38.0 (2)	5.57	35.8 (4)	12.8	3.86 (74)	289 (41)	1232 (110)	0.1369 (2)	0.569 (5)
62235#10	0.12330	1.41 (1)	1.24	11.4 (1)	12.9 (1)	27.8 (1)	34.7 (2)	5.96	36.4 (5)	12.0	5.54 (88)	332 (61)	1083 (88)	0.1367 (2)	0.598 (4)
Av. #1-#10		1.53 (1)	1.35	12.4 (1)	13.8 (1)	29.7 (1)	37.6 (3)	6.24	34.6 (5)	13.8				0.1369 (1)	0.596 (28)
Av. #6-#10		1.53 (1)	1.34	12.3 (1)	14.0 (1)	29.9 (1)	37.7 (2)	6.19	35.1 (5)	13.3	4.00 (84)	288 (43)	1069 (108)	0.1368 (2)	0.598 (40)

Re* calculated Re abundances according to $^{187}Re/^{188}Os$ ratios required for the measured $^{187}Os/^{188}Os$ ratios starting from the solar system initial of 0.09531 at 4.558 Ga (Shirey and Walker 1998). Uncertainties (2σ) on mass fractions, $^{187}Os/^{188}Os$ and $^{187}Re/^{188}Os$ ratios for aliquots are given in parentheses and refer to the last decimal places. Mass fractions of Rh and Au were determined via combined internal/external standardization and uncertainties are estimated as <10% and <15%, respectively. Tellurium, Se, and S were analyzed always in five aliquots of each sample and otherwise not analyzed (n.a.). Measurements which were affected by interferences of ZrO on Pd masses are reported as not detected (n.d.). Element mass fractions below average blank + procedural detection limit (Table S1) are reported as below detection limit (b.d.l.). Concentrations which were clearly detectable with isotope dilution ICP-MS, but overlap within uncertainties with calculated procedural detection limits are set in curly brackets (see text for further details).

[a]Approximately 80 vol% of the aqua regia solution was lost during digestion, Os, Te, Se, and S could therefore not be analyzed (consequently average mass fractions for these elements are calculated without aliquot #7).

[b]High Pt and Pd mass fractions excluded from average because they are not regarded as characteristic of the bulk sample.

[c]The HSE fractions of these aliquots were found to contain high abundances of natural Re (the resulting high Re/Os ratios are not supported by measured $^{187}Os/^{188}Os$ ratios). Averages are mass-weighted concentration data and weighted 2σ uncertainties and $^{187}Os/^{188}Os$ and $^{187}Re/^{188}Os$ ratios ($\pm 2\sigma_m$) for 10 HSE or 5 HSE + chalcogen aliquots, respectively.

$^{103}Rh/^{101}Ru$ ratios (Fischer-Gödde et al. 2010). Consistency and possible interferences were checked by comparison to results from $^{197}Au/^{195}Pt$, $^{197}Au/^{196}Pt$, and $^{103}Rh/^{193}Ir$ ratios.

Total analytical blanks (TAB) determined during the course of this study (Table S1 in supporting information) were on average (±1 SD): 1.4 ± 0.6 pg Re, 1.1 ± 0.2 pg Os ($^{187}Os/^{188}Os = 0.124 \pm 0.021$), 1.2 ± 0.7 pg Ir, 1.0 ± 0.5 pg Ru, 23 ± 12 pg Pt, 5.3 ± 3.4 pg Rh, 39 ± 18 pg Pd, 2.6 ± 1.1 pg Au ($n = 10$), and 60 ± 33 pg Te, 1.2 ± 0.8 ng Se, 2.0 ± 1.5 μg S ($n = 5$). During digestion of 15405 and 14305, a different batch of HNO_3 was used which yielded higher Os and Re blanks of 3.3 ± 0.4 pg Os with $^{187}Os/^{188}Os = 0.126 \pm 0.004$ and 4.5 ± 1.5 pg Re ($n = 4$). All concentrations were corrected for average TAB contributions, which account generally for <0.5% Os, Ir, and Ru; <1% Au; <3% Rh and Pt; <6% Re and Pd; <10% Se and S; and <18% Te of the measured amounts. Exceptions are 0.8–1% for Os and 7–12% Re in 14305 (due to higher Os and Re TAB) and Se and Te in 15405 and 15445 (see below). Based on the precision of measured isotope ratios and the uncertainty of TAB, the precision of concentration determinations for individual aliquots is estimated to be better than 0.3% for Os; 1% for Ir and Ru; 5% for Re, Pt, and Pd; 15% for S; and 20% for Se and Te (2σ). The precision of Rh and Au concentration determinations by internal/external standardization is estimated to be better than 10% and 15%, respectively.

TABs are similar to previous studies using the same analytical methods (Wang and Becker 2014; Gleißner and Becker 2017) and similar procedural detection limits were calculated (Table S1). However, the overall low concentrations of the analyzed elements and splitting into two separate fractions (when Te, Se, and S were analyzed) sometimes yielded large blank contributions and lower signal intensities. In 15405, the low HSE concentrations yield systematically higher blank contributions of 0.7–1.7% Ru, 1.4–2.6% Ir and Os, 5–10% Au, 13–30% Pt and Rh, 18–40% Pd, and 34–79% Re, resulting in concentration uncertainties (2σ) of up to 40% (Re up to 60%). In 15405 and 15445 blank contributions to Se (10–15%) and in 15445 to Te (30–40%) are higher than in other samples and blank corrected amounts overlap within uncertainties with calculated procedural detection limits. Therefore, concentration uncertainties in these cases are considerably larger (30–60%, curly brackets in Table 1).

RESULTS

Mass fractions of HSE, Te, Se, S, and $^{187}Os/^{188}Os$ ratios of the studied lunar mafic impact melt breccias are listed in Table 1 and are illustrated in Figs. 2–4 and S3 in supporting information for individual aliquots and in Figs. 5–8 for bulk rocks. Element ratios of integrated bulk samples were obtained from either regression of HSE versus Ir diagrams or calculated from weighted averages of concentration determinations in the aliquots (Tables S2 and S3 in supporting information).

Aliquots of the crystalline matrix breccia 14305 display limited variability in HSE concentrations and ratios (Fig. 2a). The Re-Os systematics appear to be complex and disturbed (Fig. 3a). Within uncertainties, six aliquots overlap a 3.93 Ga reference isochron, which might be consistent with a thermal overprint related to the Imbrium impact (Snape et al. 2016). Five of these data points show a tendency toward older ages. Remaining aliquots display higher $^{187}Re/^{188}Os$ ratios, inconsistent with measured $^{187}Os/^{188}Os$ ratios. For 14305 and 14321, a very similar crystalline matrix breccia, Herpers et al. (1973) reported variable W/Re ratios and cosmic ray induced neutron capture by ^{186}W and formation of ^{187}Re. $^{187}Re/^{185}Re$ ratios 5–23% higher than natural strongly affect our isotope dilution calculation and are the most likely explanation for the variable shift in calculated $^{187}Re/^{188}Os$ ratios. Mass fractions of S, Se, and Te in the aliquots are not correlated with Ir, but within uncertainty with each other (Fig. 4). Bulk chalcogen element concentrations overlap with the range of mafic crustal lithologies (Fig. 5) and their ratios are noncarbonaceous chondrite-like for Se/Te (24), and suprachondritic for S/Se (6800; Fig. 6). The $^{187}Os/^{188}Os$ ratio of the bulk (0.1348 ± 6) indicates a long-term suprachondritic Re/Os ratio. When compared with data for 14321 (Puchtel et al. 2008), HSE ratios and $^{187}Os/^{188}Os$ ratios are identical within uncertainty and fall in the lower range of Apollo 16 mafic impact melt breccias (group 1 and 2 of Korotev 1994; Fig. 7).

Variolithic impact melt breccia 15405 shows the lowest HSE mass fractions of the present data set and HSE-Ir correlations between aliquots are more scattered (Fig. 2b). One aliquot differs in having significantly higher concentrations of Pt and Pd, but the lowest refractory HSE content. Although compromised by larger blank contributions and high uncertainties of Se values, chalcogen mass fractions fall in the same range as data for 14305 (Fig. 4) and ratios are similarly noncarbonaceous chondrite-like for Se/Te (~20) and suprachondritic for S/Se (~6700; Fig. 6). The bulk sample displays a pattern with CI chondrite normalized concentrations increasing from refractory HSE toward more volatile Pd, Au, Te, Se, and S (Fig. 5) and shows a noncarbonaceous chondrite like $^{187}Os/^{188}Os$ ratio of 0.1282 ± 3 (Fig. 7).

Mass fractions of HSE in aliquots of the intergranular impact melt rock 15445 fall in the range of values reported by Liu et al. (2015) for a different

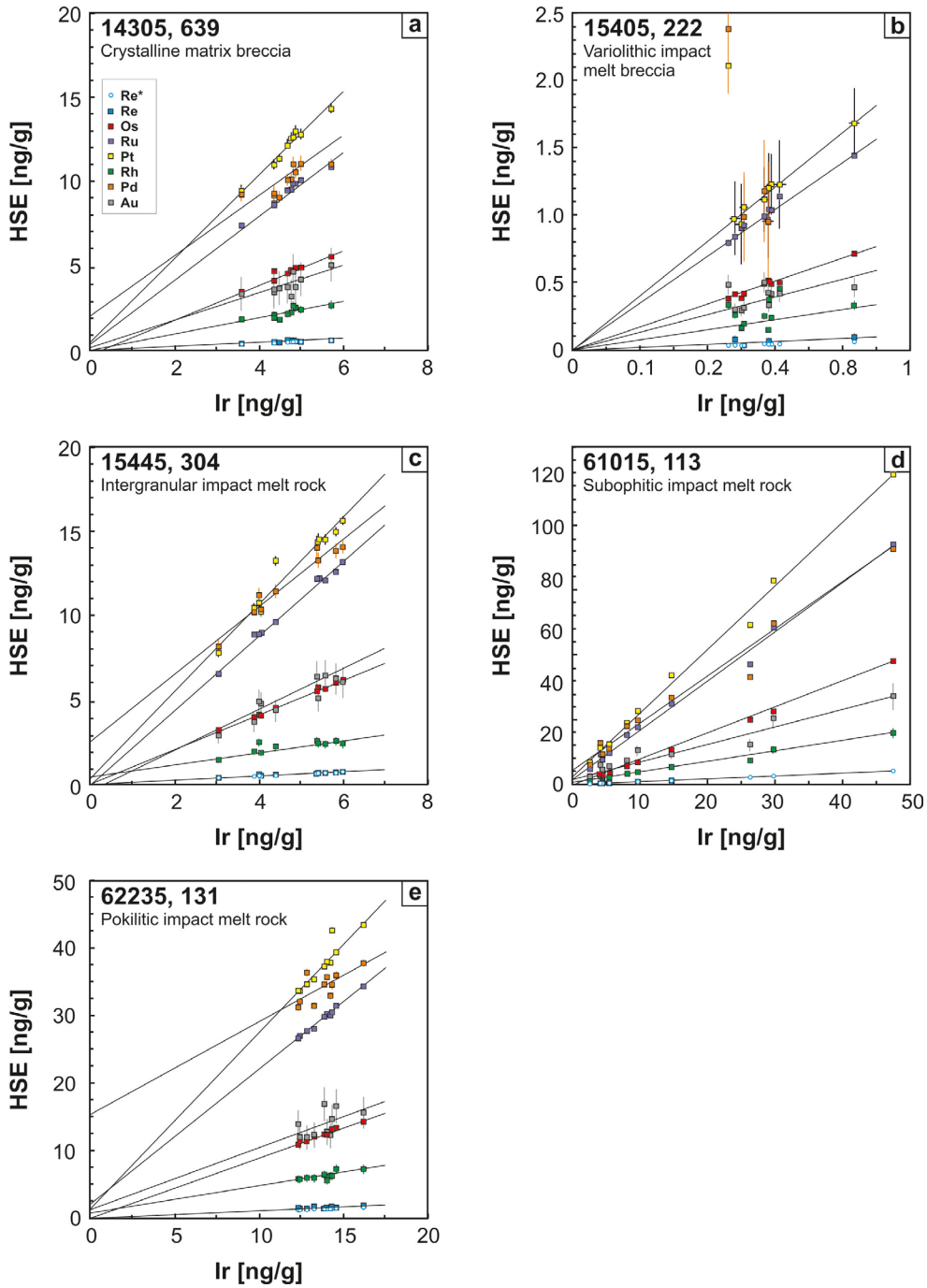

Fig. 2. Highly siderophile elements in aliquots of the studied mafic impact melt breccias. Uncertainties are displayed if larger than symbol size (2σ, note: Ir uncertainty is displayed together with Pt). Linear regression calculations are shown and intercept and slope values are given in Table S2. (Color figure can be viewed at wileyonlinelibrary.com.)

split of the same sample. However, we obtained slightly more radiogenic $^{187}Os/^{188}Os$ (Fig. 3b), indicating heterogeneous distribution of different HSE carrier phases (i.e., troilite versus Fe-Ni metal). Most aliquots of 15445 analyzed in the present study overlap with a 3.93 Ga reference isochron. Some aliquots of 15455, a similar "black and white rock" sample analyzed by Liu et al. (2015), appear consistent with formation ages >3.93 Ga. Seifert et al. (2017) reported similarly disturbed Ar-Ar release spectra for both samples and suggested a late thermal event, which could explain the deviation of aliquots from both Re-Os studies from

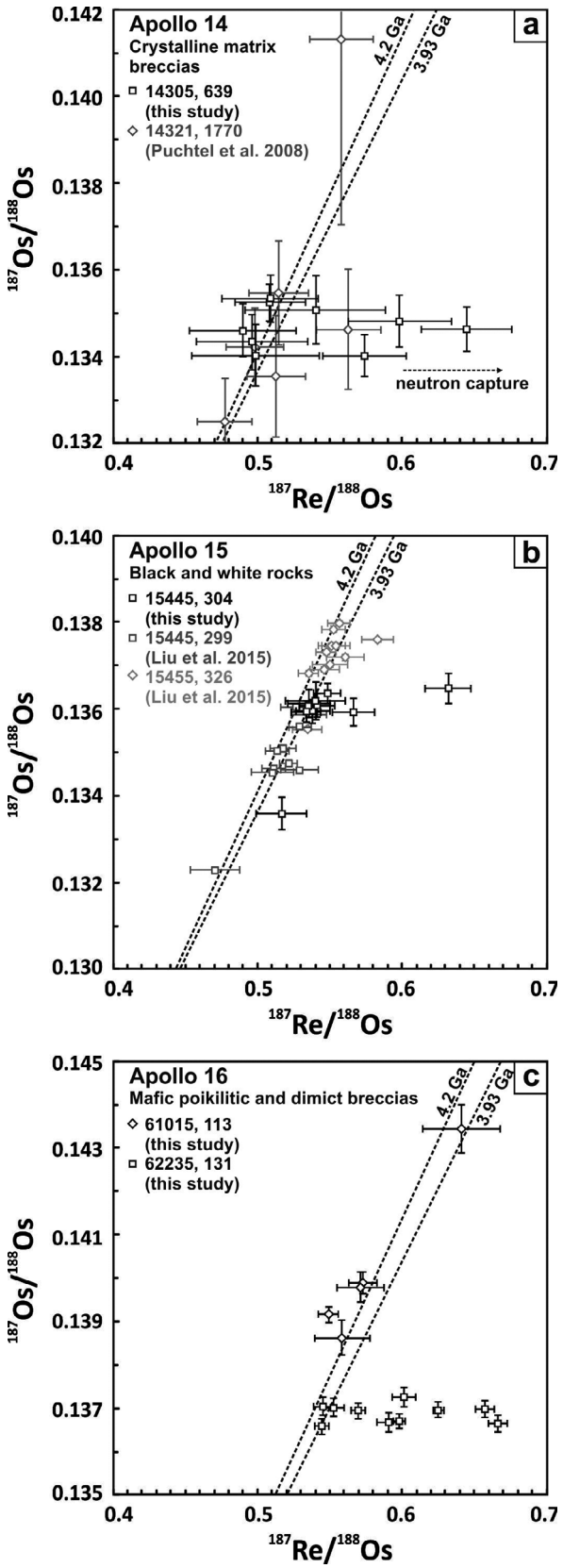

Fig. 3. Re-Os systematics in aliquots of mafic impact melt breccias (uncertainties $2\sigma_m$). Reference isochrons with chondritic initial $^{187}Os/^{188}Os$ are given according to the most likely age of the Imbrium impact (3.926 ± 2 Ga; Snape et al. 2016) and older basin-forming events recorded in impact-related zircons (~4.2 Ga; Vanderliek et al. 2019). The effect of ^{186}W neutron capture on ^{187}Re is indicated in (a) (see discussion for details).

isochronous behavior. Bulk HSE ratios of both "black and white" rocks fall into the range of Apollo 16 mafic impact melt breccias (group 1 and 2 of Korotev 1994; Fig. 7). For Se and Te, values obtained for aliquots of 15445 overlap within uncertainty with procedural detection limits. However, even considering large uncertainties, these values indicate S/Se and Se/Te ratios similar to 15405 and 14305 (Figs. 4–6).

The subophitic impact melt rock portion of dimict breccia 61015 contains abundant large Fe-Ni metal grains. Consequently, analyzed aliquots display a large range in HSE concentrations and strong correlations in a HSE versus Ir diagram (Fig. 2d). The Re-Os systematics of three of five analyzed aliquots do not overlap with a 3.93 Ga reference isochron, but show a tendency toward older ages (Fig. 3c). In all aliquots, CI chondrite normalized mass fractions of HSE increase from refractory to more volatile HSE, similar to other studied mafic impact melt breccias (Fig. S3). However, in contrast to all other studied samples, chalcogens display only slightly fractionated to unfractionated chalcogen/Ir, Se/Te (6.7–12.6), and S/Se (2400–2700) ratios, close to CI chondrite values (Fig. 4). Bulk HSE/Ir ratios and $^{187}Os/^{188}Os$ of 0.1398 ± 17 in this sample are among the highest observed for Apollo 16 mafic impact melt breccias (Fig. 7).

Different aliquots of the poikilitic impact melt rock 62235 are characterized by very similar concentrations of HSE, Te, Se, and S, and $^{187}Os/^{188}Os$ ratios (Figs. 2–4). Most aliquots display high $^{187}Re/^{188}Os$ ratios inconsistent with measured $^{187}Os/^{188}Os$ ratios. The high Re concentration of all aliquots appears inconsistent with neutron capture effects within the 5% analytical uncertainty of our concentration determinations. Instead, the disturbance of $^{187}Re/^{188}Os$ ratios is most likely the result of small-scale redistribution of Re and/or localized re-equilibration of $^{187}Os/^{188}Os$ due to later impacts (see discussion in Gleißner and Becker 2017). Chalcogens display suprachondritic ratios (Se/Te = 60–89; S/Se = 3300–4300; Fig. 4) and variable depletion when compared to HSE (Fig. S3). Bulk Se and S abundances of 62235 are somewhat higher than in 14305, 15405, and 15445, but still overlap with concentrations of these elements obtained on HSE-poor

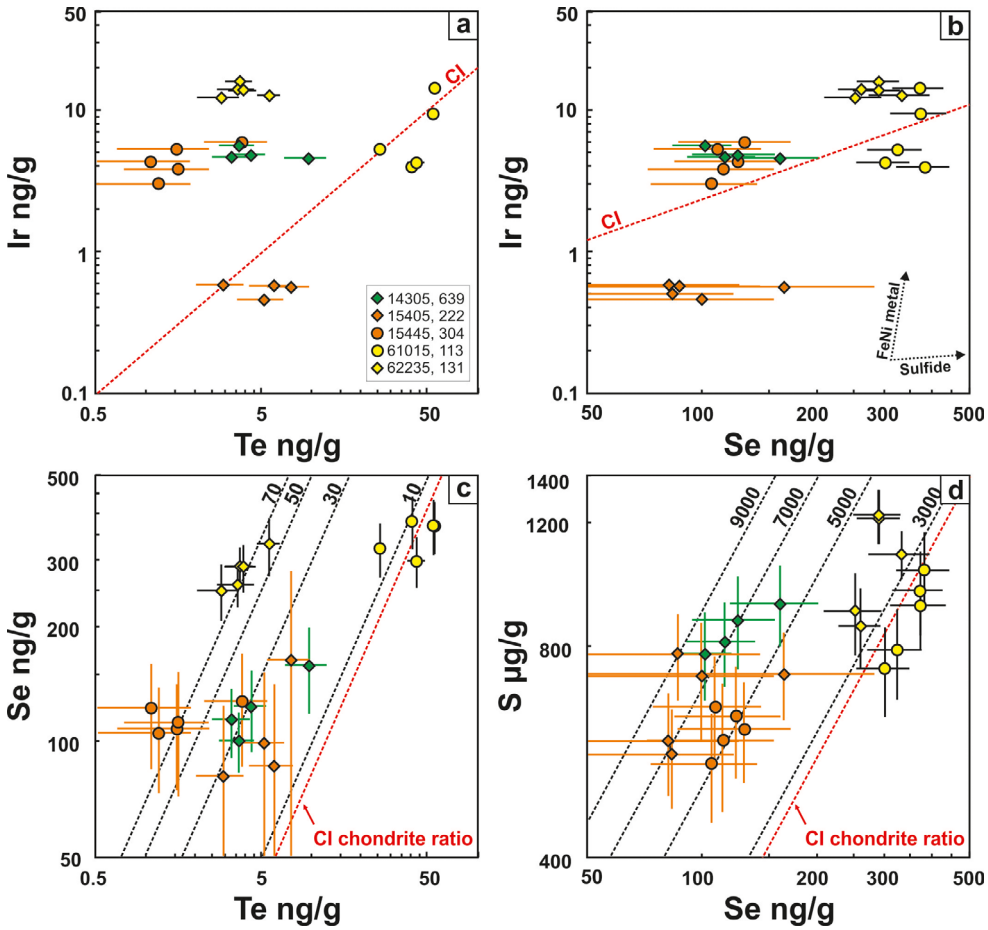

Fig. 4. The chalcogens S, Se, and Te in aliquots of studied mafic impact melt breccias (logarithmic scale, uncertainties 2σ). The contribution of different phases to observed abundances is highlighted schematically in (b). Mean CI chondrite ratios according to Lodders (2003). (Color figure can be viewed at wileyonlinelibrary.com.)

mafic crustal rocks (Fig. 5). Bulk HSE/Ir ratios and $^{187}Os/^{188}Os$ (0.1368 ± 2) fall in the range of Apollo 16 mafic impact melt breccias (group 1 and 2 of Korotev 1994; Fig. 7).

DISCUSSION

Mafic impact melt breccias are the most abundant impactite lithology among the Apollo sample suite. Their inventory of HSE is believed to preserve a compositional record of basin-forming impactors accreted after crust formation (e.g., Morgan et al. 1972). However, whether specific impactor compositions can be identified is debated. Abundances of SVE have been used tentatively as additional tracers (e.g., Morgan et al. 1974), but the behavior of these elements was often considered ambiguous (e.g., Haskin and Warren 1991). Although SVE are of great relevance for our understanding of lunar accretion and differentiation history (e.g., Steenstra et al. 2017; Righter et al. 2018), we still mostly rely on early RNAA data on lunar rocks, which have not been tested by isotope dilution ICP-MS methods. In the following, we will discuss the siderophile element inventory of mafic impact melt breccias with a focus on the distribution of the chalcogens S, Se, and Te in mafic impact melt breccias, contributions to element inventories from primary igneous rocks, constraints on impactor compositions, and processes which led to their distribution in the lunar megaregolith.

Siderophile Element Inventory of Lunar Mafic Impact Melt Breccias

The Mg- and Fe-rich major element composition of lunar mafic impact melt breccias in combination with their high incompatible element concentrations (i.e., the KREEP signature) indicates that they cannot have formed from typical anorthositic lunar crust. Instead, it has been suggested that all of them derive from impact(s)

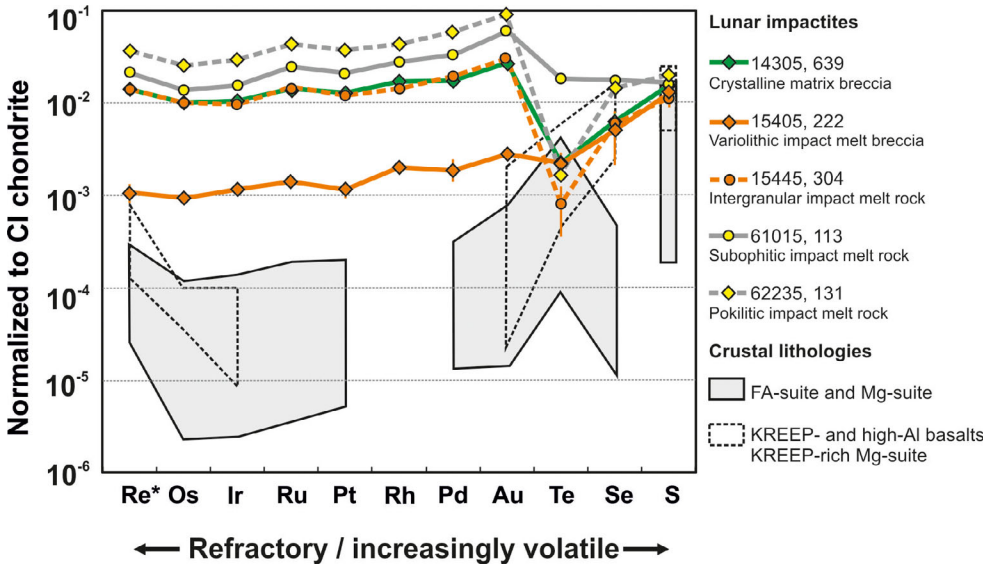

Fig. 5. Highly siderophile elements, Te, Se, and S in bulk mafic impact melt breccias. Mass fractions are normalized to CI chondrite data and elements are displayed in the order of decreasing 50% condensation temperature from a gas of solar composition (Lodders 2003). All values are weighted averages and weighted 2σ uncertainties of five rock aliquots of each sample (Table 1). Calculated Re* was used instead of measured Re concentrations (see discussion for details). Ranges of feldspathic crustal rocks and ancient mafic lithologies from isotope dilution ICP-MS data (Day et al. 2010), RNAA data (Morgan et al. 1972; Ganapathy et al. 1973; Hughes et al. 1973; Krähenbühl et al. 1973; Morgan et al. 1974, 1975; Higuchi and Morgan 1975; Gros et al. 1976; Hertogen et al. 1977; Wolf et al. 1979; Ebihara et al. 1992), and compiled S data (Haskin and Warren 1991). (Color figure can be viewed at wileyonlinelibrary.com.)

into a region of the crust that was both mafic and rich in incompatible elements, the Procellarum KREEP Terrane (Haskin et al. 1998; Korotev 2000). The compositional variability between different groups of mafic impact melt breccias is explained by a mixture of different crustal components of the pre-Imbrium Procellarum KREEP Terrane (Korotev 2000). Samples of this study are mafic impact melt rocks and breccias displaying characteristic KREEP-like lithophile trace element patterns. Their composition and diverse clast population testifies to the presence of incompatible element-depleted and enriched mafic and felsic lithologies in the target region(s) of the impact(s) (e.g., KREEP-rich and -poor basalts and impactites in 14305, KREEP basalt and alkali-suite in 15405, Mg-suite in 15445, ferroan anorthosite in 61015). Assimilation of different proportions of these endmember rock types affected the composition of lithophile trace elements in impact melts, but might have had an influence on the inventory of SVE as well.

In past RNAA studies, the analytical accuracy and precision were sometimes low for elements in the lower ng/g range and analytical blanks during chemical separation were not reported. Since samples of the Apollo missions are precious, duplicates were rarely analyzed and the analytical precision was estimated externally. For example, Keays et al. (1974) report uncertainties in the range of 35–40% (1 SD) for the reproducibility of the Te concentration in a terrestrial basalt reference material. In our study, the propagated internal precision of the isotope dilution ICP-MS measurements and the uncertainties of analytical blanks during chemical separation yield concentration uncertainties of ~20% (2σ) for Te and Se in most analyzed aliquots (Table 1). Although the splitting of the digestion aliquots into HSE and S-Se-Te fractions poses some limitations, the overall precision of concentration determinations is increased by a factor of 2–4 when compared to older data. Available RNAA Se data fall within or overlap within uncertainty with the range of concentrations obtained for different aliquots in this study. In contrast, mass fractions of Te are more variable (Table S3), but since different splits of the sample were analyzed, heterogeneity may play a role. Following the multiple aliquot approach used in recent HSE studies, in this contribution, we analyzed several rock subsamples (instead of homogenized sample powders) for S, Se, Te, and HSE mass fractions. Aliquots of the studied samples display well-defined correlations between different HSE, but also some deviations from the regression lines (Fig. 2). A similar behavior has been observed in other mafic impact melt rocks and is attributed to small-scale partitioning in the Fe-Ni-S-P system and the relative abundance of Fe-Ni

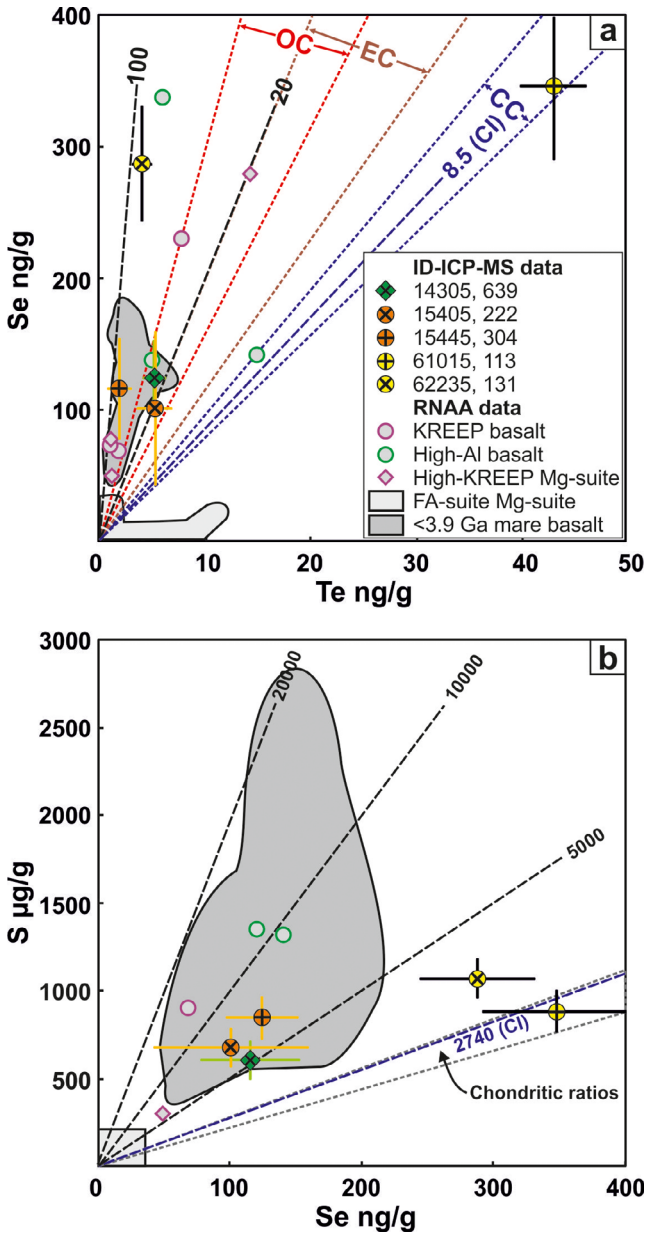

Fig. 6. a) Tellurium versus Se and (b) Se versus S concentrations in bulk mafic impact melt breccias (weighted averages and weighted 2σ uncertainties of five aliquots) compared to available data for ancient mafic lithologies and the range of feldspathic crustal rocks (references as in Fig. 5). Data for post-3.9 Ga mare basalts are from RNAA studies (Wänke et al. 1975, 1976; Wolf et al. 1979) compiled with S data from the lunar sample compendium (Meyer 2010). Ranges of Se/Te and S/Se ratios of chondrite classes are given for comparison (Wang and Becker [2013] and references therein). (Color figure can be viewed at wileyonlinelibrary.com.)

metal, schreibersite, and troilite in small aliquots (Gleißner and Becker 2017). Mass fractions of S, Se, and Te do not correlate with HSE (Figs. 4a and 4b). For example, samples that contain visible Fe-Ni metal grains (15445 and 61015) display a larger range in HSE concentrations, but not so for Te and Se. The distribution of chalcogens can be assessed from aliquots of 61015 which contain exceptionally large globules of intergrown Fe-Ni metal, schreibersite, and troilite (Fig. 1e) and display the largest variation in HSE mass fractions (Fig. 2d). Some rock aliquots display high HSE abundances and less fractionated HSE patterns (due to higher proportions of metal relative to troilite and schreibersite), whereas others are characterized by stronger fractionations (higher proportions of sulfides; see also discussion in Gleißner and Becker 2017). Although the range of chalcogen element abundances is smaller than for HSE, aliquots displaying characteristic features of Fe-Ni metal contain slightly more Te, but not more Se and S, than aliquots dominated by sulfide (Fig. S3f). Based on the limited data available, we argue that Te is more compatible in Fe-Ni metal than Se and S, which is consistent with the relative siderophile behavior of these elements (Rose-Weston et al. 2009; Steenstra et al. 2017). In the crystalline matrix breccia 14305 and the impact melt breccia 15405, no Fe-Ni metal has been reported and chalcogens in these samples are most likely controlled by the abundance of troilite. For reasons discussed in Gleißner and Becker (2017), we use mass-weighted concentration and element ratio data (instead of linear regressions, Table S2) in the following discussion.

Mass fractions of HSE in 14305, 15445, and 62235 are two to three orders of magnitude higher than in pristine crustal rocks (Fig. 5). The HSE ratios are very similar to each other and fall into the range of other mafic impact melt breccias (Fig. 7). Together with impact melt breccia 15405, which displays lower HSE contents, the impactites are characterized by similar mass fractions of S, Se, and Te with moderate variations in their ratios (Se/Te 20–72; S/Se 3700–6800). The ratios, however, are significantly more fractionated than in most chondrites (Se/Te 7.7–30; S/Se 2260–2780). When compared to RNAA data for pristine lunar rocks, impactites of the present study overlap with the range observed for pre-3.9 Ga KREEP-basalts, high-Al basalts, and some KREEP-rich Mg-suite rocks (Figs. 5 and 6). Although available data on mafic crustal lithologies, older than the majority of lunar near side basins, are limited, the latter lithologies unanimously display fractionated Se/Te ratios from 20 to 80 and S/Se ratios from 6000 to 13,300. These values are similar to post-3.9 Ga mare basalts for which more data are available. In contrast, mass fractions of Se and Te in pristine ferroan anorthosites and Mg-suite rocks are below 10 ng g^{-1} and Se/Te ranges from 0.1 to 10 (Fig. 6). Norite samples which contain higher fractions of KREEP component (i.e., trapped

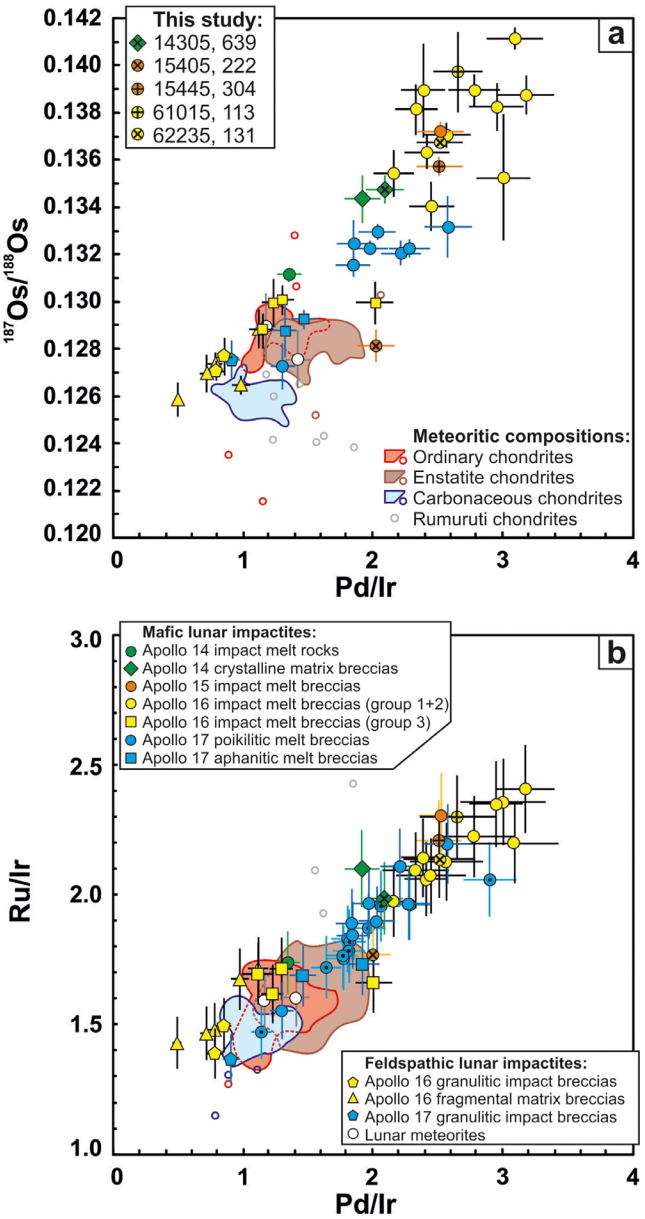

Fig. 7. a) Pd/Ir versus $^{187}Os/^{188}Os$ and (b) Pd/Ir versus Ru/Ir ratios of mafic and feldspathic lunar impactites. Bulk impactite HSE/Ir ratios are calculated from multiple aliquot data of this study and the literature (Puchtel et al. 2008; Fischer-Gödde and Becker 2012; Sharp et al. 2014; Liu et al. 2015; Gleißner and Becker 2017, 2019). Available data for Apollo 17 poikilitic impact melt breccias, obtained from homogenized powders (Norman et al. 2002) are denoted with a black dot centered in the symbol. Uncertainties of bulk impactite element ratios reflect the propagation of average 2σ uncertainties of concentration determinations and $2\sigma_m$ of $^{187}Os/^{188}Os$ ratios. Ranges of chondrite classes are given for comparison (Horan et al. 2003; Fischer-Gödde et al. 2010; Van Acken et al. 2011). Rumuruti-class chondrites and other chondrite compositions which deviate strongly from class averages are displayed individually as circles of the same color (chondrite samples showing unusual high abundances of metal and sulfide or shock alteration were excluded). (Color figure can be viewed at wileyonlinelibrary.com.)

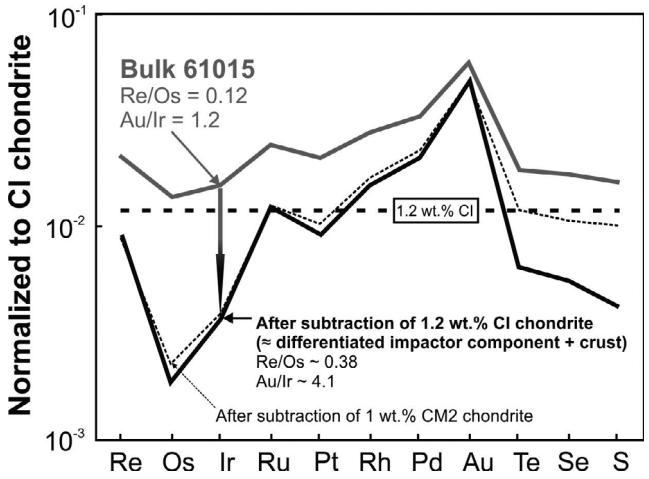

Fig. 8. Bulk composition of impact melt rock 61015 and model calculations of chondritic and differentiated impactor components (see text for details). Chondrite data from Lodders (2003), Fischer-Gödde et al. (2010), and Wang and Becker (2013).

intercumulus liquid) clearly display elevated abundances of Se when compared to other Mg-suite rocks and their Se/Te ratios fall in the range of basalts. Therefore, consistent with petrographic observations and the major and lithophile trace element composition, the inventory of chalcogen elements in the four studied breccias is controlled by ancient mafic lithologies in the target region of the impact(s). In contrast, the impact melt rock portion of 61015 displays higher and unfractionated S, Se, and Te abundances, which cannot be explained by known crustal compositions (Figs. 5 and 6), but indicates incorporation of primitive carbonaceous chondrite-like material (see discussion below).

Mafic impact melt breccias are enriched in lithophile trace elements; therefore, KREEP assimilation might have affected the inventory of chalcogens as well. However, in contrast to lithophile elements, concentrations of chalcogens in the KREEP component are uncertain. The published urKREEP estimate for S is 1100 μg g^{-1} (Warren 1989), overlapping with mass fractions in mare basalt (Haskin and Warren 1991). For Se and Te, which were not considered in KREEP estimates, no significant difference is discernible in abundances and element ratios between KREEP basalts, ancient high-Al basalts, and post-3.9 Ga mare basalts (Fig. 6). The absence of systematic differences in chalcogen element abundances between incompatible element-enriched and depleted basalts implies that the inventory of S, Se, and Te in mafic impact melt breccias is not controlled by the proportion of KREEP component, but more likely by the composition of the preexisting mafic crust.

Volatility of S-Se-Te in Lunar Impactites and Igneous Rocks

According to shock experiments and modeling of high-velocity impacts onto planetary surfaces, impactors are expected to melt and partly vaporize a larger portion of the target rock (Pierazzo and Melosh [2000] and references therein). Evidence for fractional vaporization and condensation during impacts on the lunar surface have been found in volatile element-depleted lunar impact glasses (e.g., Warren 2008) and such depletions were also reproduced in experiments (Yakovlev et al. 2011). In principle, the latter processes could also affect siderophile elements of different volatility and could impose strong fractionations; however, no such data were reported and many aspects of the dynamics and kinetics of impact-generated vapor-melt clouds are not fully understood. Therefore, it is currently not possible to quantitatively estimate the effect of large-scale impact vaporization and condensation processes on the siderophile element inventory of impactites. It is noteworthy that, Se/Te and S/Se in most studied impactites are strongly fractionated, but resemble ratios of unshocked mafic lunar lithologies (Fig. 6). This indicates melting of such materials during large impacts and recycling of their element inventory (see discussion above) or, alternatively, requires similar igneous fractionation processes that control the siderophile volatile element inventory of mafic impact melts.

After the decompression and crater modification stage, newly formed impact melts (i.e., molten crustal and impactor material) are subject to cooling and degassing of volatile components in a temperature range similar to erupted lunar volcanic rocks. Sulfur is an important volatile component of mafic magmas and degassing of chalcogen elements is a common feature in terrestrial basaltic volcanism (Edmonds and Mather 2017). However, in contrast to H_2O-rich terrestrial conditions, the most abundant gas species in the more reduced lunar igneous systems are CO, H_2, H_2S, and S_2 and minor COS, HCl, and HF (e.g., Tartese et al. 2013; Wetzel et al. 2015). Therefore, speciation and transport of elements may differ greatly from observations on Earth (Renggli et al. 2017).

Vesicles are common features of lunar basalts and impact melt rocks (Fig. 1), providing evidence for the formation of significant volume of gas at low pressure. Under reduced lunar conditions, Se and Te will most likely form trace selenide and telluride compounds which dissolve in more abundant FeS and possibly in Fe-Ni metal. Sulfur is degassed mainly as H_2S and S_2 and similar species might control the volatilization of Se and Te, although recent thermodynamic calculations for lunar gas compositions do not consider such trace compounds (Bell et al. 2015; Wing and Farquhar 2015; Renggli et al. 2017). Several lines of evidence argue for only moderate degassing of S (and by inference Se and Te) during cooling and solidification of mare basalts or impact melt sheets. First, reduced species will dominate the partitioning between melt and gas phase under the low oxygen fugacity conditions of lunar melts (Brounce et al. 2019). Shallow degassing of reduced sulfur as H_2S is consistent with thermodynamic analysis of metasomatic fluid-mineral reactions (Bell et al. 2015) and limited fractionation of S isotopes in lunar mare basalts (Wing and Farquhar 2015). The degree of S loss inferred from these studies is moderate to low (on average <10%, occasionally up to 40–60%). Second, experimental constraints that were used to propose strong degassing of S under lunar conditions (Ustunisik et al. 2015) might have been partly compromised by the presence of H_2O in experimental starting compositions. Furthermore, very strong degassing of S contradicts the relatively high S abundances in lunar igneous rocks and impactites (e.g., Wänke et al. [1975, 1976]; Haskin and Warren [1991] and this study). Third, the behavior of Se and Te is only indirectly assessable; however, lunar samples affected by fumarolic activity (i.e., condensation of a magmatic vapor phase) are usually strongly enriched in elements like Cd, In, and Tl, but less in Se and they are not enriched in Te (Krähenbühl et al. 1973; Ebihara et al. 1992). Based on these assessments, we suggest that fractionations between S, Se, and Te in the studied mafic impact melt breccias dominantly reflect processes during the formation of the primary lunar crustal lithologies and in a few cases contributions from impactors.

Composition of Impactors

Using modern mass spectrometry in combination with isotope dilution and combined isotope dilution-external standardization for monoisotopic elements such as Rh and Au, sub ng/g quantities of all HSE can be determined and small variations between sample aliquots and between different samples can be resolved (e.g., Liu et al. 2015; Gleißner and Becker 2017). However, whether the observed variations of HSE mass fractions in lunar impactites reflect distinct basin-forming events and specific impactor compositions (Norman et al. 2002; Puchtel et al. 2008; Sharp et al. 2014; Liu et al. 2015) or result from large-scale mixing of multiple ancient impactor compositions (Fischer-Gödde and Becker 2012; Gleißner and Becker 2017, 2019) is still discussed.

If the proposed large-scale mixing of different ancient impactor components is correct (see discussion

below), the broad correlation of HSE ratios defined by the suite of lunar impactites indicates that most mafic impact melt breccias contain two dominant impactor components, which differ in HSE ratios (Fig. 7). High abundances of Fe-Ni metal and HSE, observed most prominently in Apollo 16 mafic impact melt rocks and breccias, are interpreted as a signature of a common metal-rich impactor. The observed fractionation of HSE is consistent with solid metal–liquid metal partitioning similar to known magmatic iron meteorites and implies that a fragment, or several related fragments, of a planetesimal or embryo core was accreted (Korotev 1994,2000; Fischer-Gödde and Becker 2012; Liu et al. 2015; Gleißner and Becker 2017). Gleißner and Becker (2017) further constrained the large-scale fractional crystallization process that most likely produced the evolved HSE signature, but the size of the accreted core fragment and what happened to the less evolved portion remains unknown. Irrespective of these uncertainties, available data show that mafic impact melt breccias of the Apollo sample collection are all characterized by common fractionations of HSE (e.g., suprachondritic Re/Os, Ru/Pt, Pd/Ir, and Au/Ir ratios) which clearly demonstrates that their HSE inventories are biased by a common impactor component with a composition similar to differentiated metal. Tracing of small fractions of more primitive impactor compositions is therefore difficult if only HSE are considered. When compared to HSE, chalcogen element concentrations in magmatic irons are low (Shimamura et al. 1993; Wasson et al. 2007) and their contribution to the impactite inventory is therefore assumed to be minor. Chalcogen elements are abundant in primitive meteorites and display distinct fractionations between carbonaceous (Se/Te = 7.7–9.5; S/Se = 2260–2780) and noncarbonaceous (Se/Te = 11–30; S/Se = 2320–2600) chondrites (e.g., Wang and Becker [2013]; Wang et al. [2015]; Braukmüller et al. [2019] and references therein). Therefore, if primitive impactor contributions are large enough to be resolved from target rock compositions and the effect of degassing is small, chalcogen element abundances could be helpful indicators of different types of chondrites.

Most mafic impact melt breccias of the present study are characterized by chalcogen element abundances in the upper range of pristine mafic crustal lithologies and display strongly fractionated Se/Te and S/Se ratios (Fig. 6). Hence, contributions from primitive impactor compositions, if any, seem to be very small and preclude any further discrimination. In contrast to all other studied samples, the impact melt rock portion of 61015 displays a characteristically fractionated HSE pattern, as commonly observed in mafic impact melt breccias, but almost unfractionated chalcogen element abundances (Fig. 5). According to James et al. (1984), the impact melt in 61015 was formed in the floor of an expanding crater cavity and was then injected into the underlying bedrock. Rapid cooling after dike emplacement at depth likely prevented significant outgassing, consistent with incomplete degassing of highly volatile Ar from impact melt portions of Apollo 16 dimict breccias (Norman et al. 2010). Therefore, we argue that volatile loss of chalcogens appears even less likely and that dimict breccia 61015 preserved a particularly good record of its impact melt composition. Its average Se/Te of 8.0 ± 1.4 and S/Se of 2530 ± 540 overlap with the range in carbonaceous chondrites of Se/Te from 7.7 to 9.5 and S/Se from 2260 to 2780 (e.g., Wang and Becker [2013]; Wang et al. [2015]; Braukmüller et al. [2019] and references therein). To our knowledge, such a combination of siderophile element compositions does not occur in any primitive or differentiated meteorite. Therefore, we interpret the observed element distribution as direct evidence for mixing of carbonaceous chondrite-like and iron meteorite-like impactor compositions and subsequent homogenization of their siderophile element inventories during impact melt formation. We note that the detailed chronology of this mixing process cannot be directly retrieved from the sample. For instance, it is possible that the impact event that produced the measured composition of the impact melt delivered one of the above-mentioned impactor compositions into target rock that was already contaminated by the other impactor material. However, the amount and composition of chondritic and nonchondritic impactor components in 61015 can be estimated. Observed Se/Te and S/Se ratios are within the range of carbonaceous chondrites (Fig. 6) whereas chalcogen/Ir ratios fall in the restricted range of CI chondrites (Fig. 4). From the latter observations, we infer that much of the siderophile element inventory of 61015 was contributed from an impactor component with CI chondrite-like element abundances.

Following the above reasoning, we assume that the observed siderophile abundances reflect the admixture of a CI chondrite-like and a differentiated impactor component to the lunar crust and their homogenization during impact melt formation without loss of these elements (Fig. 8). Mass fractions of Os and Ir pose an upper limit of ~1.4 wt% onto the amount of the hypothetical CI chondrite-like impactor component in the mixture. Less than 1 wt% of a CI chondrite impactor component would yield unrealistically high mass fractions of chalcogens in the remaining fraction, which is interpreted to reflect the integrated composition of the differentiated impactor component (mainly HSE) and the lunar crust (some Te, Se, and S).

Assuming a CI chondrite-like impactor component of ~1.2 wt% yields remaining chalcogens partly overlapping with the range of mass fractions in crustal lithologies, but different from fractionations observed in mafic impactites (Fig. 5). Subtracting a similar amount of HSE by means of a moderately volatile depleted CM-like impactor component yields higher remaining mass fractions of chalcogens and is therefore regarded as rather unlikely. The discrepancy of the remaining chalcogen pattern between 61015 and the other mafic impactites might be explained by a mixture of mafic and feldspathic target compositions to form the very high aluminous impact melt. Alternatively, and in contrast to arguments provided in the previous section, stronger degassing of Te from impact melt pools (as opposed to impact melt veins) could explain the difference as well. This, however, cannot be constrained without further knowledge about the volatility of chalcogens under lunar conditions. At the current stage, we argue that preferred partitioning of Te into metal (as discussed above) might have caused a bias toward slightly higher bulk Te concentrations in aliquots of 61015. In contrast to the chalcogens, it is noteworthy that fractionations of the HSE in the remaining fraction are more pronounced and resemble characteristics of the proposed differentiated impactor component in mafic impact melt rocks and breccias (e.g., suprachondritic Re/Os, Ru/Pt, Pd/Ir; and Au/Ir; Gleißer and Becker 2017). In spite of the uncertainties of this approach, the model is able to explain the trace element composition of the sample and is consistent with available data for lunar crustal rocks and meteorites.

The significance of the above finding is twofold. First, at the scale of an impact melt sheet, mixing and homogenization of different impactor signatures is an important process. This is consistent with the proposed large-scale mixing model of Fischer-Gödde and Becker (2012) and needs to be considered for chemical tracing of impactor material in lunar impactites. Second, the identification of undifferentiated impactor material (most likely CI chondrite-like) confirms the accretion of volatile-rich material. This is important because ancient lunar impactites might contain traces of the same impactor population that was accreted late to Earth. Ratios and abundances of S, Se, Te, and HSE in terrestrial peridotites are consistent with the view that the bulk silicate Earth accreted 0.4–0.7 wt of slightly volatile-depleted, carbonaceous chondrite-like material after core formation (Wang and Becker 2013). Based on recent Se isotope measurements, Varas-Reus et al. (2019) proposed that the composition of the bulk silicate Earth can be explained if the late accreted material was dominantly CI-type carbonaceous chondrite-like and of lower mass than previously estimated (0.12–0.18 wt%). Although this would be a surprisingly good match with our interpretation of CI chondrite-like material in a lunar impactite, the available Se isotope data for chondrites allow the alternative conclusion of a larger mass fraction of bulk carbonaceous chondrite material of different groups accreted to Earth.

Constraints on the Accretion and Mixing History of Impactor Material

Mafic impact melt breccias with a meteoritic siderophile element component characterized by suprachondritic Au/Ir ratios (i.e., the differentiated metal signature) have been reported from various Apollo landing sites. Their common abundance in ejecta deposits of the lunar nearside and their KREEP-rich lithophile trace element composition led to the hypothesis that virtually all of them originate from the Procellarum KREEP Terrane and were formed as a consequence of a single iron meteorite projectile that formed the Imbrium basin (e.g., Haskin et al. 1998; Korotev 2000). In this model, the range in Ar-Ar ages from 3.7 to 4.0 Ga has been explained with uncertainties in the interpretation of disturbed ^{40}Ar-^{39}Ar degassing spectra and the accuracy with which measured portions of mafic impact melt breccias may have recorded the time of their formation (Haskin et al. 1998). The currently accepted age of the Imbrium impact is based on the formation of crystalline matrix breccias of the Fra Mauro Formation at the Apollo 14 landing site. Snape et al. (2016) determined ^{207}Pb-^{206}Pb ages of phosphates ranging from 3.926 to 3.944 Ga, interpreted as reflecting complete to partial resetting of the U-Pb system due to heating related to the Imbrium event. In combination with ages of KREEP-rich mafic impact melt breccias from other landing sites, an average age of 3.926 ± 0.002 Ga was interpreted to represent the most likely age for the Imbrium impact (Snape et al. 2016; Thiessen et al. 2018). Highly siderophile element data, which provide the most robust indication of impactor material in impactites, are available for the two Fra Mauro breccias 14305 (this study) and 14321 (Puchtel et al. 2008). In both breccias, the isotopic composition of osmium and relative abundances of HSE (Fig. 7) are very similar, and in conjunction with age data, they provide constraints on the time when the differentiated metal component was accreted. Because the phosphate ^{207}Pb-^{206}Pb dates range from the presumed age of Imbrium (3.926 Ga) to somewhat older ages of up to 3.944 Ga, Snape et al. (2016) argued that the Imbrium impact led to brecciation and heating of older KREEP-rich Fra Mauro impactites,

which were originally formed by one or several previous impact events at or before 3.944 Ga. Recently, Thiessen et al. (2019) described zircons within different crystalline impactite clasts of 14305 and 14321. Petrographic observations led to the conclusion that some zircons are cogenetic with other minerals of the assemblage (i.e., the zircons are not mineral clasts). In situ dating of these zircons yield ^{207}Pb-^{206}Pb ages of 4.216 ± 0.005 Ga and 4.166 ± 0.013 Ga, which is considerably older than the proposed age of the Imbrium impact. Aphanitic impactite microbreccias, which are the most common constituents of clasts and matrix, dominate the HSE inventory of these impactites (Morgan et al. 1972; Puchtel et al. 2008; this study). If the HSE-rich aphanites existed before, as indicated by the pre-Imbrian Pb-Pb ages, and the rocks simply underwent further brecciation, the brecciation event (presumably related to the formation of Imbrium) did not contribute significant impactor material. We, therefore, conclude that HSE in both breccias record the addition of impactor material to the aphanitic microbreccia lithology in an earlier impact event rather than during the Imbrium impact.

If the above reasoning is correct, the formation age of the aphanitic microbreccia lithology in Fra Mauro breccias would constrain the minimum age for the accretion of the differentiated metal component. Although HSE concentrations and zircon ages were not determined on the same impactite clasts, the ages determined by Thiessen et al. (2019) could represent formation ages of the microbreccia lithologies which dominate the inventory of lithophile and siderophile trace elements of both breccias (see discussion above). Furthermore, we note that the described assemblages of zircon, phosphate, and occasional K-feldspar are consistent with crystallization from KREEP-rich impact melts. Although some uncertainties on the exact age of the impact remain, based on petrographic observations and HSE compositions of Apollo 14 crystalline matrix breccias, the differentiated metal signature does not represent the composition of the projectile that produced the Imbrium basin. Apparently the Re-Os systematics of Apollo 14 breccias were not completely re-equilibrated during the last thermal overprint at 3.926–3.944 Ga. Some aliquots of both samples are consistent with a pre-3.93 Ga formation age (Fig. 3a). However, large uncertainties and the strong effect of cosmic ray induced neutron capture on Re preclude any conclusive age constraints. Based on an Re-Os isochron age, Fischer-Gödde and Becker (2012) proposed a formation age of 4.21 ± 0.13 Ga for the KREEP-rich mafic impact melt breccia 67935, which also displays the characteristic HSE pattern of the differentiated metal component. Recent work, however, suggests that this isochron may have been biased toward older ages by undigested clasts (Haber and Scherer 2018), and thus, the precise delivery time of the metal component is still uncertain.

Once formed, impactites are exposed to impact gardening that produces a mixed megaregolith. Fischer-Gödde and Becker (2012) have suggested that large-scale mixing of the differentiated metal and the undifferentiated meteorite-like components may explain the variation of HSE ratios in mafic impact melt breccias from different landing sites. This is also consistent with recent modeling approaches of Michael et al. (2018) and Liu et al. (2019), which show that large impacts, which produced significant volume of melt, should leave a trace in the near-surface material until the present day, but that high-frequency smaller impacts can change the local melt component in the near surface. Impact-induced mingling of clasts of different lithologies and impactor components on the scale of individual samples have been demonstrated clearly by siderophile element studies on clasts and matrix of lithic impact breccias like the North Ray crater fragmental matrix breccias (Hertogen et al. 1977; Gleißner and Becker 2019). However, in order to explain the observed age distribution in mafic impact melt breccias, the model requires that clastic mixtures have been homogenized by melting and crystallized as clast-poor impact melt rocks (e.g., Michael et al. 2018; Liu et al. 2019). The latter process is apparently more difficult to prove because the amount of pre-existing impactites and the nature of their inherited meteoritic component are unknown. The presence of fractionated HSE compositions (i.e., the differentiated metal impactor component) and unfractionated chalcogen element compositions (i.e., a primitive impactor component) in the homogeneous impact melt rock portion of 61015 provides evidence for such chemical mixing on the scale of individual impact melt sheets (see discussion above). Similar examples of impactites with mixed impactor heritage might be found by further studies of a larger range of siderophile elements in mafic impact melt breccias. For example, many mafic impact melt breccias of the Apollo 16 sample suite display similarly fractionated HSE patterns (Fischer-Gödde and Becker 2012; Liu et al. 2015; Gleißner and Becker 2017; this study), but according to recent Ar-Ar dates were formed in different melt-producing impact events (Norman et al. 2006; Niihara et al. 2019). This further supports the hypothesis that the Imbrium impact excavated pre-existing KREEP-rich mafic impactites and because of its young age contributed predominantly to ejecta deposits at all landing sites, but not necessarily dominates their HSE budget.

SUMMARY AND CONCLUSIONS

The first combined data set on mass fractions of S, Se, Te, and HSE in lunar impactites reveals insights into the variable distribution of siderophile elements in mafic impact melt breccias and their potential to constrain the composition of impactor material. The most outstanding result is the detection of CI chondrite-like impactor material in one of the studied samples. Unfractionated Se/Te, S/Se, and Te/Ir ratios in 61015 indicate the incorporation of ~1 wt% primitive impactor material with CI chondrite-like siderophile element abundances. The latter example demonstrates that primitive impactor components in polymict impactites can be identified by combining HSE and S-Se-Te data and provides evidence for mixing and homogenization of different impactor components in lunar impact melt sheets. Mass fractions and ratios of S, Se, and Te of other impactites closely resemble those of pristine mafic crustal rocks like pre-3.9 Ga lunar basalts. Therefore, we conclude that mafic target rocks contributed a large fraction of their S-Se-Te inventory to the budget of these elements in the impactites. This, however, complicates the detection of small amounts of impactor material, especially if the impactor was depleted in volatile elements and/or had fractionated Se/Te ratios like in noncarbonaceous chondrites.

Mafic impact melt breccias from different Apollo landing sites are characterized by relatively high HSE abundances and fractionated HSE patterns with suprachondritic Re/Os, Ru/Pt, Pd/Ir, and Au/Ir ratios. This characteristic HSE pattern can be attributed to the accretion of larger quantities of differentiated planetesimal core material (Fischer-Gödde and Becker 2012; Gleißner and Becker 2017). The differentiated metal component likely was accreted to the Procellarum KREEP Terrane before the Imbrium impact. The Re-Os systematics of crystalline matrix breccias from the Fra Mauro Formation at Apollo 14 is consistent with a pre-Imbrian (i.e., >3.93 Ga) delivery of the differentiated metal onto a mafic and KREEP-rich target region and later incorporation of KREEP-rich mafic impactite clasts into impact breccias of Imbrian age. Impact gardening led to a large-scale distribution of the differentiated metal component and mixing with basin ejecta with broadly chondritic HSE compositions at the Apollo 14, 15, 16, and 17 landing sites (Gleißner and Becker 2017, 2019). Consequently, the HSE inventory of many mafic impact melt breccias appears to be biased by variable amounts of the differentiated metal component. Because of the high and strongly fractionated HSE abundances of the latter component, the nature of primitive impactor material in polymict impactites cannot be determined from HSE alone. At least in some cases, mass fractions of S, Se, and Te can help, because they were less influenced by the composition of the differentiated metal impactor component.

Acknowledgments—The authors wish to thank CAPTEM and the Lunar Sample Curator for sample allocation, Z. Wang for inspiring discussions and development of S-Se-Te separation techniques, and F. Mangels and T. Roth for performing some of the chemical separations in the laboratory. Furthermore, we acknowledge constructive reviews by F. Wombacher and the Associated Editor I. Leya. J. Liu and two anonymous reviewers provided helpful comments on an earlier version of this manuscript. This work was funded by the Deutsche Forschungsgemeinschaft (BE1820/11-1, SFB-TRR 170, subproject B1-1). This is TRR 170 Publication No. 112. The authors declare no conflicts of interest. Open access funding enabled and organized by Projekt DEAL.

Editorial Handling—Dr. Ingo Leya

REFERENCES

Becker H., Morgan J. W., Walker R. J., MacPherson G. J., and Grossman J. N. 2001. Rhenium-osmium systematics of calcium-aluminium-rich inclusions in carbonaceous chondrites. *Geochimica et Cosmochimica Acta* 65:3379–3390.

Bell A. S., Shearer C. K., Maarten deMoor J. and Provencio P. 2015. Using the sulfide replacement petrology in lunar breccia 67915 to construct a thermodynamic model of S-bearing fluid in the lunar crust. *Geochimica et Cosmochimica Acta* 171:50–60.

Braukmüller N., Wombacher F., Funk C., and Münker C. 2019. Earth's volatile element depletion pattern inherited from a carbonaceous chondrite-like source. *Nature Geoscience* 12:564–568.

Brounce M., Boyce J., McCubbin F. M., Humphreys J., Reppart J., Stolper E., and Eiler J. 2019. The oxidation state of sulfur in lunar apatite. *American Mineralogist* 104:307–312.

Carlson I. C. and Walton W. J. A. 1978. *Apollo 14 rock samples*. JSC 14240. Houston, Texas: NASA Johnson Space Center. 413 p.

Chu Z. Y., Yan Y., Chen Z., Guo J. H., Yang Y. H., Li C. F., and Zhang Y. B. 2015. A comprehensive method for precise determination of Re, Os, Ir, Ru, Pt, Pd concentrations and Os isotopic compositions in geological samples. *Geostandards and Geoanalytical Research* 39:151–169.

Day J. M. D. and Walker R. J. 2015. Highly siderophile element depletion in the Moon. *Earth and Planetary Science Letters* 423:114–124.

Day J. M. D., Walker R. J., James O. B., and Puchtel I. S. 2010. Osmium isotope and highly siderophile element systematics of the lunar crust. *Earth and Planetary Science Letters* 289:595–605.

Ebihara M., Wolf R., Warren P. H., and Anders E. 1992. Trace-elements in 59 mostly highland moon rocks.

Proceedings, 22nd Lunar and Planetary Science Conference. pp. 417–426.
Edmonds M. and Mather T. A. 2017. Volcanic sulfides and outgassing. *Elements* 13:105–110.
Fischer-Gödde M. and Becker H. 2012. Osmium isotope and highly siderophile element constraints on ages and nature of meteoritic components in ancient lunar impact rocks. *Geochimica et Cosmochimica Acta* 77:135–156.
Fischer-Gödde M., Becker H., and Wombacher F. 2010. Rhodium, gold and other highly siderophile element abundances in chondritic meteorites. *Geochimica et Cosmochimica Acta* 74:356–379.
Ganapathy R., Morgan J. W., Krähenbühl U., and Anders E. 1973. Ancient meteoritic components in lunar highland rocks: Clues from trace elements in Apollo 15 and 16 samples. Proceedings, Lunar and Planetary Science Conference. pp. 1239–1261.
Gleißner P. and Becker H. 2017. Formation of Apollo 16 impactites and the composition of late accreted material: Constraints from Os isotopes, highly siderophile elements and sulfur abundances. *Geochimica et Cosmochimica Acta* 200:1–24.
Gleißner P. and Becker H. 2019. Origin of lunar fragmental matrix breccias—Highly siderophile element constraints. *Meteoritics & Planetary Science* 54:2006–2026.
Grange M. L., Nemchin A. A., and Pidgeon R. T. 2013. The effect of 1.9 and 1.4 Ga impact events on 4.3 Ga zircon and phosphate from an Apollo 15 melt breccia. *Journal of Geophysical Research: Planets* 118:2180–2197.
Gros J., Takahashi H., Hertogen J., Morgan J. W., and Anders E. 1976. Composition of the projectiles that bombarded the lunar highlands. Proceedings, 7th Lunar Science Conference. pp. 2403–2425.
Haber T. and Scherer E. 2018. The age of lunar impact melt rock 67935–Imbrium or not? (abstract #360). 12th European Planetary Science Congress.
Haskin L. and Warren P. H. 1991. Lunar chemistry. In *Lunar sourcebook*, edited by Heiken G. H., Vaniman D. T., and French B. M. Cambridge: Cambridge University Press. pp. 357–474.
Haskin L., Korotev R. L., Rockow K. M., and Jolliff B. L. 1998. The case for an Imbrium origin of the Apollo thorium-rich impact-melt breccias. *Meteoritics & Planetary Science* 33:959–975.
Hauri E. H., Saal A. E., Rutherford M. J., and Van Orman J. A. 2015. Water in the Moon's interior: Truth and consequences. *Earth and Planetary Science Letters* 409:252–264.
Herpers U., Herr W., Kulus H., Michel R., Thiel K., and Woelfle R. 1973. Manganese-53 profile, particle track studies and the rhenium-187 isotopic anomaly of breccia 14305. Proceedings, 4th Lunar Science Conference. pp. 2157–2169.
Hertogen J., Janssens M.-J., Takahashi H., Palme H., and Anders E. 1977. Lunar basins and craters–Evidence for systematic compositional changes of bombarding population. Proceedings, 8th Lunar and Planetary Science Conference. pp. 17–45.
Higuchi H. and Morgan J. W. 1975. Ancient meteoritic component in Apollo 17 boulders. Proceedings, 6th Lunar and Planetary Science Conference. pp. 1625–1651.
Horan M. F., Walker R. J., Morgan J. W., Grossman J. N., and Rubin A. E. 2003. Highly siderophile elements in chondrites. *Chemical Geology* 196:27–42.
Hughes T., Keays R., and Lovering J. 1973. Siderophile and volatile trace elements in Apollo 14, 15, and 16 rocks and fines: Evidence for extralunar component and Tl-, Au-, and Ag-enriched rocks in the ancient lunar crust (abstract). Proceedings, 4th Lunar Science Conference. pp. 400–402.
James O. B., Flohr M. K., and Lindstrom M. M. 1984. Petrology and geochemistry of lunar dimict breccia 61015. Proceedings, 15th Lunar and Planetary Science Conference. pp. C63–C86.
Keays R. R., Ganapathy R., Laul J., Krähenbühl U., and Morgan J. W. 1974. The simultaneous determination of 20 trace elements in terrestrial, lunar and meteoritic material by radiochemical neutron activation analysis. *Analytica Chimica Acta* 72:1–29.
Korotev R. L. 1994. Compositional variation in Apollo 16 impact-melt breccias and inferences for the geology and bombardment history of the Central Highlands of the Moon. *Geochimica et Cosmochimica Acta* 58:3931–3969.
Korotev R. L. 2000. The great lunar hot spot and the composition and origin of the Apollo mafic ("LKFM") impact-melt breccias. *Journal of Geophysical Research: Planets* 105:4317–4345.
Krähenbühl U., Ganapathy R., Morgan J. W., and Anders E. 1973. Volatile elements in Apollo 16 samples: Implications for highland volcanism and accretion history of the moon. Proceedings, 4th Lunar and Planetary Science Conference. pp. 1325–1348.
Lindstrom M. M., Marvin U. B., Vetter S. K., and Shervais J. W. 1988. Apennine front revisited-diversity of Apollo 15 highland rock types. Proceedings, 18th Lunar and Planetary Science Conference. pp. 169–185.
Liu J. G., Sharp M., Ash R. D., Kring D. A., and Walker R. J. 2015. Diverse impactors in Apollo 15 and 16 impact melt rocks: Evidence from osmium isotopes and highly siderophile elements. *Geochimica et Cosmochimica Acta* 155:122–153.
Liu T., Michael G., Engelmann J., Wünnemann K., and Oberst J. 2019. Regolith mixing by impacts: Lateral diffusion of basin melt. *Icarus* 321:691–704.
Lodders K. 2003. Solar system abundances and condensation temperatures of the elements. *The Astrophysical Journal* 591:1220–1247.
Luck J.-M. and Allègre C. J. 1983. ^{187}Re–^{187}Os systematics in meteorites and cosmochemical consequences. *Nature* 302:130–132.
McGee P., Simonds C., Warner J., and Phinney W.1979. Introduction to the Apollo collections: Part 2: Lunar breccias. JSC 15013. Houston, Texas: NASA Johnson Space Center. 206 p.
Meyer C. 2010. Lunar sample compendium (abstract #1016). 41st Lunar and Planetary Science Conference. CD-ROM.
Michael G., Basilevsky A., and Neukum G. 2018. On the history of the early meteoritic bombardment of the Moon: Was there a terminal lunar cataclysm? *Icarus* 302:80–103.
Morgan J. W., Laul J., Krähenbühl U., Ganapathy R., and Anders E. 1972. Major impacts on the Moon: Characterization from trace elements in Apollo 12 and 14 samples. Proceedings, 3rd Lunar Science Conference. pp. 1377–1395.
Morgan J. W., Ganapathy R., Higuchi H., Krähenbühl U., and Anders E. 1974. Lunar basins-tentative characterization of projectiles, from meteoritic elements in Apollo 17 boulders. Proceedings, 5th Lunar and Planetary Science Conference. pp. 1703–1736.

Morgan J. W., Higuchi H., and Anders E. 1975. Meteoritic material in a boulder from the Apollo 17 site: Implications for its origin. *The Moon* 14:373–383.

Niihara T., Beard S. P., Swindle T. D., Schaffer L. A., Miyamoto H., and Kring D. A. 2019. Evidence for multiple 4.0–3.7 Ga impact events within the Apollo 16 collection. *Meteoritics & Planetary Science* 54:675–698.

Norman M. D., Bennett V. C., and Ryder G. 2002. Targeting the impactors: Siderophile element signatures of lunar impact melts from Serenitatis. *Earth and Planetary Science Letters* 202:217–228.

Norman M. D., Duncan R. A., and Huard J. J. 2006. Identifying impact events within the lunar cataclysm from 40Ar-39Ar ages and compositions of Apollo 16 impact melt rocks. *Geochimica et Cosmochimica Acta* 70:6032–6049.

Norman M. D., Duncan R. A., and Huard J. J. 2010. Imbrium provenance for the Apollo 16 Descartes terrain: Argon ages and geochemistry of lunar breccias 67016 and 67455. *Geochimica et Cosmochimica Acta* 74:763–783.

Pierazzo E. and Melosh H. 2000. Hydrocode modeling of oblique impacts: The fate of the projectile. *Meteoritics & Planetary Science* 35:117–130.

Puchtel I. S., Walker R. J., James O. B., and Kring D. A. 2008. Osmium isotope and highly siderophile element systematics of lunar impact melt breccias: Implications for the late accretion history of the Moon and Earth. *Geochimica et Cosmochimica Acta* 72:3022–3042.

Reimold W. and Borchardt R. 1984. Subophitic lithologies in KREEP-rich poikilitic impact melt rocks from Cayley Plains, Apollo 16—Remnants of a volcanic highland crust? *Earth and Planetary Science Letters* 67:9–18.

Renggli C., King P., Henley R., and Norman M. 2017. Volcanic gas composition, metal dispersion and deposition during explosive volcanic eruptions on the Moon. *Geochimica et Cosmochimica Acta* 206:296–311.

Renne P. R., Swisher C. C., Deino A. L., Karner D. B., Owens T. L., and DePaolo D. J. 1998. Intercalibration of standards, absolute ages and uncertainties in $^{40}Ar/^{39}Ar$ dating. *Chemical Geology* 145:117–152.

Righter K., Pando K., Marin N., Ross D., Righter M., Danielson L., Lapen T., and Lee C. 2018. Volatile element signatures in the mantles of Earth, Moon, and Mars: Core formation fingerprints from Bi, Cd, In, and Sn. *Meteoritics & Planetary Science* 53:284–305.

Rose-Weston L., Brenan J. M., Fei Y. W., Secco R. A., and Frost D. J. 2009. Effect of pressure, temperature, and oxygen fugacity on the metal-silicate partitioning of Te, Se, and S: Implications for earth differentiation. *Geochimica et Cosmochimica Acta* 73:4598–4615.

Ryder G. and Bower J. 1977. Petrology of Apollo 15 black-and-white rocks 15445 and 15455-Fragments of the Imbrium impact melt sheet. Proceedings, Lunar and Planetary Science Conference. pp. 1895–1923.

Seifert L., Kring A., and Swindle T. 2017. ^{40}Ar-^{39}Ar dating of lunar impact melts—Searching for Imbrium (abstract #2993). 48th Lunar and Planetary Science Conference.

Sharp M., Gerasimenko I., Loudin L. C., Liu J. G., James O. B., Puchtel I. S., and Walker R. J. 2014. Characterization of the dominant impactor signature for Apollo 17 impact melt rocks. *Geochimica et Cosmochimica Acta* 131:62–80.

Shervais J. W., Taylor L. A., and Laul J. 1983. Ancient crustal components in the Fra Mauro breccias. Proceedings, Lunar and Planetary Science Conference. pp. B177–B192.

Shimamura T., Takahashi T., Honda M., and Nagai H. 1993. Multi-element and isotopic analyses of iron meteorites using a glow discharge mass spectrometer. *Journal of Analytical Atomic Spectrometry* 8:453–460.

Shirey S. B. and Walker R. J. 1998. The Re-Os isotope system in cosmochemistry and high-temperature geochemistry. *Annual Review of Earth and Planetary Sciences* 26:423–500.

Snape J. F., Nemchin A. A., Grange M. L., Bellucci J. J., Thiessen F., and Whitehouse M. J. 2016. Phosphate ages in Apollo 14 breccias: Resolving multiple impact events with high precision U-Pb SIMS analyses. *Geochimica et Cosmochimica Acta* 174:13–29.

Spudis P., Ryder G., Taylor G., Keil K., and McCormick K. 1991. Sources of mineral fragments in impact melts 15445 and 15455–Toward the origin of low-K Fra Mauro basalt. Proceedings, 21st Lunar and Planetary Science Conference. pp. 151–165.

Steenstra E., Lin Y., Dankers D., Rai N., Berndt J., Matveev S., and Westrenen W. 2017. The lunar core can be a major reservoir for volatile elements S, Se, Te and Sb. *Scientific Reports* 7:1–8.

Tartese R., Anand M., Barnes J. J., Starkey N. A., Franchi I. A., and Sano Y. 2013. The abundance, distribution, and isotopic composition of hydrogen in the Moon as revealed by basaltic lunar samples: Implications for the volatile inventory of the Moon. *Geochimica et Cosmochimica Acta* 122:58–74.

Thiessen F., Nemchin A., Snape J., Bellucci J., and Whitehouse M. J. 2018. Apollo 12 breccia 12013: Impact-induced partial Pb loss in zircon and its implications for lunar geochronology. *Geochimica et Cosmochimica Acta* 230:94–111.

Thiessen F., Nemchin A., Snape J., and Whitehouse M. J. 2019. U-Pb SIMS ages of Apollo 14 zircon: Identifying distinct magmatic episodes. *Meteoritics & Planetary Science* 54:1720–1736.

Ustunisik G., Nekvasil H., Lindsley D. H., and McCubbin F. M. 2015. Degassing pathways of Cl-, F-, H-, and S-bearing magmas near the lunar surface: Implications for the composition and Cl isotopic values of lunar apatite. *American Mineralogist* 100:1717–1727.

Van Acken D., Brandon A. D., and Humayun M. 2011. High-precision osmium isotopes in enstatite and Rumuruti chondrites. *Geochimica et Cosmochimica Acta* 75:4020–4036.

Vanderliek D., Becker H., and Rocholl A.2019. Large-scale redistribution of heterogeneous PKT material by the imbrium impact—Evidence from petrology and U-Pb zircon dating of a complex Apollo 16 Breccia (abstract #2379). 50th Lunar and Planetary Science Conference. CD-ROM.

Varas-Reus M. I., König S., Yierpan A., Lorand J.-P., and Schoenberg R. 2019. Selenium isotopes as tracers of a late volatile contribution to Earth from the outer solar system. *Nature Geoscience* 12:779–782.

Walker R. J., Bermingham K., Liu J. G., Puchtel I. S., Touboul M., and Worsham E. A. 2015. In search of late-stage planetary building blocks. *Chemical Geology* 411:125–142.

Wang Z. C. and Becker H. 2013. Ratios of S, Se and Te in the silicate Earth require a volatile-rich late veneer. *Nature* 499:328–332.

Wang Z. C. and Becker H. 2014. Abundances of sulfur, selenium, tellurium, rhenium and platinum-group elements

in eighteen reference materials by isotope dilution sector-field ICP-MS and Negative TIMS. *Geostandards and Geoanalytical Research* 38:189–209.

Wang Z. C., Becker H., and Wombacher F. 2015. Mass Fractions of S, Cu, Se, Mo, Ag, Cd, In, Te, Ba, Sm, W, Tl and Bi in geological reference materials and selected carbonaceous chondrites determined by isotope dilution ICP-MS. *Geostandards and Geoanalytical Research* 39:185–208.

Wänke H., Palme H., Baddenhausen H., Dreibus G., Jagoutz E., Kruse H., Palme C., Spettel B., Teschke F., and Thacker R. 1975. New data on the chemistry of lunar samples-Primary matter in the lunar highlands and the bulk composition of the moon. Proceedings, 6th Lunar Science Conference. pp. 1313–1340.

Wänke H., Palme H., Kruse H., Baddenhausen H., Cendales M., Dreibus G., Hofmeister H., Jagoutz E., Palme C., and Spettel B. 1976. Chemistry of lunar highland rocks—A refined evaluation of the composition of the primary matter. Proceedings, 7th Lunar Science Conference. pp. 3479–3499.

Warren P. H. 1989. KREEP: major-element diversity, trace-element uniformity (almost). Workshop on Moon in Transition: Apollo 14, KREEP, and Evolved Lunar Rocks Proceedings. pp. 149–153.

Warren P. H. 2008. Lunar rock-rain: Diverse silicate impact-vapor condensates in an Apollo-14 regolith breccia. *Geochimica et Cosmochimica Acta* 72:3562–3585.

Wasson J. T., Huber H., and Malvin D. J. 2007. Formation of IIAB iron meteorites. *Geochimica et Cosmochimica Acta* 71:760–781.

Wetzel D. T., Hauri E. H., Saal A. E., and Rutherford M. J. 2015. Carbon content and degassing history of the lunar volcanic glasses. *Nature Geoscience* 8:755–758.

Wing B. A. and Farquhar J. 2015. Sulfur isotope homogeneity of lunar mare basalts. *Geochimica et Cosmochimica Acta* 170:266–280.

Wolf R., Woodrow A., and Anders E. 1979. Lunar basalts and pristine highland rocks–Comparison of siderophile and volatile elements. Proceedings, 10th Lunar and Planetary Science Conference. pp. 2107–2130.

Yakovlev O., Gerasimov M., and Dikov Y. P. 2011. Estimation of temperature conditions for the formation of HASP and GASP glasses from the lunar regolith. *Geochemistry International* 49:213–223.

SUPPORTING INFORMATION

Additional supporting information may be found in the online version of this article.

Fig. S1. Lithophile trace element data for samples of this study (literature).

Fig. S2. Siderophile trace element data for samples of this study (literature).

Fig. S3. Siderophile trace element concentrations in multiple aliquots (this study).

Table S1. Total analytical blank values.

Table S2. Element ratios in bulk samples of this study.

Table S3. Comparison of S, Se, and Te with literature data.